

Perseus ALMA Chemistry Survey (PEACHES). I. The Complex Organic Molecules of Embedded Protostars

YAO-LUN YANG,^{1,2} NAMI SAKAI,² YICHEN ZHANG,² AYA E. HIGUCHI,³ NADIA M. MURILLO,² SHAOSHAN ZENG,² ZIWEI ZHANG,² MUNEAKI IMAI,⁴ TAKESHI SAKAI,⁵ ANA LÓPEZ-SEPULCRE,⁶ YOKO OYA,⁴ YOSHIMASA WATANABE,⁷ TOMOYA HIROTA,³ SATOSHI YAMAMOTO,⁴ CECILIA CECCARELLI,⁶ AND BERTRAND LEFLOCH⁶

¹Department of Astronomy, University of Virginia, Charlottesville, VA 22904-4235, USA

²RIKEN Cluster for Pioneering Research, Wako-shi, Saitama, 351-0106, Japan

³National Astronomical Observatory of Japan, Osawa, Mitaka, Tokyo 181-8588, Japan

⁴Department of Physics, The University of Tokyo, 7-3-1, Hongo, Bunkyo-ku, Tokyo 113-0033, Japan

⁵Department of Communication Engineering and Informatics, Graduate School of Informatics and Engineering,

The University of Electro-Communications, Chofugaoka, Chofu, Tokyo 182-8585, Japan

⁶Univ. Grenoble Alpes, CNRS, Institut de Planétologie et d’Astrophysique de Grenoble (IPAG), F-38000 Grenoble, France

⁷Shibaura Institute of Technology, 3-9-14 Shibaura, Minato-ku, Tokyo 108-8548, Japan

1. INTRODUCTION

Planet formation may start during the embedded phase of star formation. In the scenario where planets form from the embedded disks, resulting in substructures, the chemistry of embedded disks may play a significant role for the chemical composition of the forming planets. In the recent years, observations discover the emission of unsaturated complex organic molecules such as carbon-chain molecules (e.g., Sakai & Yamamoto 2013; Sakai et al. 2014; Law et al. 2018) and the saturated complex organic molecules (COMs, Cazaux et al. e.g., 2003; Bottinelli et al. e.g., 2007; Jørgensen et al. e.g., 2020) toward the center of several protostellar cores, indicating that embedded protostars have developed a complex chemistry at the disk-forming region. The saturated organic molecules have single covalent bonds for all atoms, making them rich in hydrogen, while the unsaturated organic molecules contain double or triple bonds between carbon atoms, making them poor in hydrogen. If the forming planets inherit the chemistry of embedded disks, the abundance of complex organic molecules may implicate future developments of organics on the planets.

Heavier or more complex molecules, such as cyclic-C₃H₂, SO, and complex organic molecules (COMs), are in the gas phase at the inner protostellar envelope ($T \gtrsim 100$ K), which coincidentally corresponds to ~ 100 au for typical low-mass protostars (Yang et al. 2020). Thus, COMs exclusively trace the properties of the inner envelope where a disk may be forming (Aikawa

2013; Sakai et al. 2014). The kinematics of a rotating infalling envelope has been analyzed with the observations of heavier or more complex molecules, such as CH₃OH and CH₂DOH for HH 212 (Lee et al. 2017), CS for IRAS 04365+2535 (Sakai et al. 2016) and L483 (Oya et al. 2017), cyclic-C₃H₂ for L1527 (Sakai et al. 2014), OCS for IRAS 16293–2422 A (Oya et al. 2016), and methanol and HCOOH for B335 (Imai et al. 2019).

While recent observations show several embedded protostars with rich spectra of complex molecules, the occurrence of complex molecules at embedded protostars and its relationship to the star formation process remain poorly understood. Several protostars are rich in COMs but show little emission of long carbon-chain molecules, such as IRAS 16293–2422 (Jørgensen et al. 2016), NGC 1333 IRAS 4A (Bottinelli et al. 2004; Sahu et al. 2019), and B335 (Imai et al. 2016, 2019); some protostars are rich in long carbon-chain molecules but not in COMs, such as L1527 (Sakai et al. 2010) and IRAS 15398–3359 (Sakai et al. 2009). While the bimodal chemical appearance hints a bimodal evolutionary path, the chemical pathways of complex molecules at the embedded protostars remain ill-constrained as a few protostars show the emission of both COMs and long carbon-chain molecules at different scales, such as L483 (Oya et al. 2017). Recent surveys show lack of correlations between COMs and long carbon-chain molecules, suggesting that observational biases may contribute to the apparent bimodal chemistry (Graninger et al. 2016; Higuchi et al. 2018) (reference).

Perseus molecular cloud is one of the most active nearby star-forming region, which extends ~ 10 pc on the sky. Infrared and submillimeter surveys reveal more than 400 young stellar objects as well as ~ 100 dense cores, which contains ~ 50 Class 0 and I proto-

stars (Hatchell et al. 2005; Jørgensen et al. 2008; Dunham et al. 2013; hereafter the embedded protostars). The Perseus molecular cloud contains star-forming regions in a wide range of environments. The majority of protostars in Perseus are associated with two clusters, NGC 1333 and IC 348. NGC 1333 has significant outflow activity (reference) and a younger age than that of IC 348. The embedded protostars associated with IC 348 lie at the southwest of IC 348 near a prominent outflow, HH 211 (reference). Most of other embedded protostars at Perseus are related to L1448, L1455, Bernard 1 (B1), and Bernard 5 (B5). L1448 has active outflows that may regulate the ongoing star formation (Curtis et al. 2010); The protostars in L1455 are slightly more evolved than that in other regions; (reference) B1 exhibits rich spectra of deuterated species (reference). Thus, the Perseus molecular cloud provides the ideal test bed for chemistry in embedded protostars by surveying the protostars within each region and across the entire cloud.

Higuchi et al. (2018) presented a pilot survey of the chemistry in the Perseus embedded protostars with Nobeyama 45m telescope, which survey all Class 0/I protostars (Hatchell et al. 2007) that have the bolometric luminosity (L_{bol}) greater than 1 L_{\odot} (0.7 L_{\odot} for protostars in B1 and B5) and the envelope mass greater than 1 M_{\odot} . This pilot survey probes the molecules such as C₂H, c-C₃H₂, and CH₃OH and find the majority of the sources are neither only rich in CH₃OH or carbon-chain molecules. They also suggest a possible correlation between the location of sources within the clouds and the chemistry. Other surveys with single-dish telescopes also characterize the COMs abundance at embedded protostars and test the chemical models (e.g., Bergner et al. 2017). Due to the large beam, chemistry survey with single-dish telescopes often more sensitive to COMs in cool temperature (10–20 K), which may not be directly associated with the COMs thermally desorbed from icy grains. Interferometry is crucial for probing the warm COMs at embedded protostars. With 26 embedded protostars from several star-forming regions, Belloche et al. (2020) find CH₃OH in about half of the sample as well as other more complex COMs. They also investigate the potential origin of COMs and reveal apparent chemical difference among multiple systems. Despite of the growing sample of COMs detections in embedded protostars, the statistics of COMs occurrence and abundance remain unconstrained due to the biases from the source selection and the limited resolution. To unbiasedly survey the chemistry, we conducted the Perseus ALMA Chemistry Survey (PEACHES) that probes the complex chemistry toward Perseus embedded protostars. The source selection follows the same criteria as Higuchi

et al. (2018) with a few pointing modifications using the results from the VLA Nascent Disk and Multiplicity Survey (VANDAM) of Perseus protostars (Tobin et al. 2016).

Section 2 describes the details of our ALMA observations. Section XXX

2. OBSERVATIONS

The PEACHES observations were conducted in two ALMA projects (2016.1.01501.S and 2017.1.01462.S; PI: N. Sakai), surveying 37 fields toward the Perseus molecular cloud. Table 1 lists the details about the ALMA projects used in this study. ALMA correlator was configured to have 13 spectral windows (spw) at Band 6, which have 12 narrow spws with 480 channels and a wide spw with 980 channels. The narrow spws were tuned to observe specific molecular species, such as SiO, CS, CH₃OH and CH₃CN, with a spectral resolution of 122 kHz ($\sim 0.15 \text{ km s}^{-1}$), while the wide spw aimed to observe the continuum with a resolution of 0.976 MHz ($\sim 0.4 \text{ km s}^{-1}$). The frequency setup for the two ALMA projects are largely identical except for the wide continuum window (spw04), which shifts by ~ 620 MHz. Table 2 lists the frequency ranges for each spw.

We use CASA (McMullin et al. 2007) for standard calibration and imaging of the continuum and spectral lines with `tclean`. Because of the rich spectra, we manually flag the lines for the continuum imaging. The spectra of spw10 and spw11 are combined for the imaging because the broad SiO emission. The spectra is cleaned down to 0.022 Jy, except for the spw04, which is cleaned down to 0.008 Jy due to its lower spectral resolution. The line imaging used the “multiscale” deconvolver with a robust parameter of 0.5, because the targeted emission traces different spatial scales (e.g. SiO for outflows and COMs for the inner envelope/disk).

The synthesized beam is about $0.^{\prime\prime}6 \times 0.^{\prime\prime}4$ (Table 3). The Perseus molecular cloud is not at a single distance. Many studies assume a distance of 235 pc for Perseus based on the maser observations toward NGC 1333 SVS 13 (Hirota et al. 2008). Recently, Ortiz-León et al. (2018) derive a distance of 321 ± 10 pc for IC 348 using VLBA and a distance of 293 ± 22 pc for NGC 1333 using *Gaia* parallaxes. Zucker et al. (2020) combine the *Gaia* parallaxes and photometric data with a Bayesian framework to revise the distances toward different sightlines of Perseus, resulting in distances ranging from 234 pc to 331 pc. In this study, we assume a distance of 300 pc for the entire Perseus cloud. Thus, the synthesized beam is about $180 \text{ au} \times 120 \text{ au}$.

3. ANALYSES

Table 1. ALMA Projects for PEACHES

Project code	Observation time	Amplitude calibrator	Bandpass calibrator	Phase calibrator
2016.1.01501.S	2016-11-16, 19, 26, 29, 30	J0238+1636	J0237+2848	J0336+3218
2017.1.01462.S	2018-09-10, 12	J0237+2848	J0237+2848	J0336+3218

Table 2. Frequency Setup

	Spectral window		2016.1.01501.S		2017.1.01462.S	
		frequency range		frequency range		channel width
spw00		243.483–243.542 GHz	122.070 kHz	243.502–243.561 GHz	122.070 kHz	
spw01		243.878–243.937 GHz	122.070 kHz	243.897–243.956 GHz	122.070 kHz	
spw02		244.200–244.259 GHz	122.070 kHz	244.219–244.278 GHz	122.070 kHz	
spw03		244.898–244.957 GHz	122.070 kHz	244.917–244.975 GHz	122.070 kHz	
spw04		246.186–247.124 GHz	976.562 kHz	245.805–246.743 GHz	976.562 kHz	
spw05		257.489–257.548 GHz	122.070 kHz	257.509–257.568 GHz	122.070 kHz	
spw06		258.218–258.276 GHz	122.070 kHz	258.238–258.296 GHz	122.070 kHz	
spw07		259.288–259.347 GHz	122.070 kHz	259.308–259.366 GHz	122.070 kHz	
spw08		258.974–259.032 GHz	122.070 kHz	258.993–259.052 GHz	122.070 kHz	
spw09		262.046–262.104 GHz	122.070 kHz	262.066–262.124 GHz	122.070 kHz	
spw10_spw11 ^a		260.442–260.551 GHz	122.070 kHz	260.462–260.571 GHz	122.070 kHz	
spw12		261.787–261.845 GHz	122.070 kHz	261.807–261.865 GHz	122.070 kHz	

^a The spectra of spw10 and spw11 are combined to measure the baseline due to the broad SiO emission.

3.1. Identification of Young Stellar Object

In the 37 field of view, 51 continuum peaks are identified. We use the CASA task `imfit` to iteratively fit for continuum sources down to 5σ of the residual image within the central 70% of the primary beam size ($20''$). For the field centered on Per-emb 16, the fitting uses a threshold of 4σ and extends the mask to the entire primary beam as a continuum source, Per-emb 28, is detected toward the edge of the primary beam where the noise is elevated. The continuum of the multiple systems are manually fitted to the individual continuum peak. Two protostars, L1448 IRS 2E and SVS 3, become non-detection in our observations due to their low brightness. SVS 13C locates at the edge of the primary beam, resulting in a noisy continuum. Thus, we exclude SVS 13C from this study, making a total of 50 protostars. **L1448 IRS 2E has CS emission.**

Figure 1 shows the continuum emission along with the fitted shapes, while Table 3 lists the properties of the continuum sources. The continuum emission peak appears as a compact circular or elliptical shape. Some sources show extended continuum emission resembling the shape of outflow cavities, such as Per-emb 22 A and B. Three sources, EDJ2009-237, Per-emb 60, and EDJ2009-172, show no spectral line and no reliable measurement of source velocity in literature; therefore, we

exclude them from spectral extraction as well as the line identification and modeling. However, these three sources still contribute to the total number of sources for calculating the detection statistics.

The observations resolve or marginally resolve 90% (45 of 50) of the continuum sources. Our sample includes single sources as well as resolved and unresolved multiple systems. According to the VANDAM survey (Tobin et al. 2016), our sample contains eleven binary systems and one triple system. Two of eleven binary systems are resolved and the triple system appears as a single source and an unresolved binary. In total, 20% of the sources are unresolved binary.

Tychoniec et al. (2020) derive the central dust mass of Perseus protostars using the 9 mm VLA observations (VANDAM; see Table 3). Dust emission from the center of a protostar may be marginally optically thick at millimeter wavelengths (Ko et al. 2020), making the derived dust mass lower limits. Seven sources in our sample have the averaged continuum brightness temperature exceeding 10 K (Table 3). NGC 1333 IRAS 4A1 has a T_b of 21.9 K, the brightest among our sample. In fact, continuum opacity limits the detectability of COMs toward 4A1, where COMs appear as absorption at ALMA Band 7 (Sahu et al. 2019) and emission at centimeter wavelengths (De Simone et al. 2020). Toward the other

Table 3. PEACHES Sample

Source	Common names	R.A. (J2000)	Decl. (J2000)	v_{lsr}	Ref. (v_{lsr})	Beam	Cont. Size	T_{cont}	$M_{\text{dust}}^{\text{a}}$
		(hh:mm:ss)	(dd:mm:ss)	(km s $^{-1}$)	($''$)	($''$)	(K)	(M $_{\oplus}$)	
Per-emb 22 B		03:25:22.35	30:45:13.11	4.3	S19	0''64×0''39	0''95×0''51	0.92	23.1±13.0
Per-emb 22 A		03:25:22.41	30:45:13.26	4.3	S19	0''64×0''39	0''86×0''65	1.71	96.4±24.1
L1448 NW	L1448 IRS 3C	03:25:35.67	30:45:34.16	4.2	H18	0''64×0''39	0''83×0''47	3.15	382.4±54.9
Per-emb 33 B/C		03:25:36.32	30:45:15.19	5.3	S19	0''64×0''39	0''75×0''48	5.55	226.4±43.7
Per-emb 33 A		03:25:36.38	30:45:14.72	5.3	S19	0''64×0''39	0''73×0''45	10.33	294.0±57.6
L1448 IRS 3A		03:25:36.50	30:45:21.90	4.6	H18	0''64×0''39	0''85×0''59	3.21	235.1±47.8
Per-emb 26		03:25:38.88	30:44:05.28	5.4	S19	0''64×0''39	0''69×0''45	8.03	636.1±102.5
Per-emb 42		03:25:39.14	30:43:57.90	5.8	S19	0''64×0''39	0''64×0''39	0.66	116.5±29.0
Per-emb 25	IRAS 03235+3004	03:26:37.51	30:15:27.81	5.5	S18	0''64×0''39	0''69×0''41	5.27	172.6±65.4
Per-emb 17	L1455 IRS 1, IRAS 03245+3002	03:27:39.11	30:13:02.96	6.0	S19	0''64×0''40	0''79×0''48	2.00	199.4±34.0
Per-emb 20	L1455 IRS 4	03:27:43.28	30:12:28.88	5.3	S19	0''64×0''40	1''29×0''78	0.14	<31.1±15.5
L1455 IRS 2		03:27:47.69	30:12:04.33	5.1	H18	0''64×0''40	0''60×0''38	0.13	23.3±13.3
Per-emb 35 A	NGC 1333 IRAS 1	03:28:37.10	31:13:30.77	7.4	Y20	0''66×0''42	0''75×0''51	0.93	47.0±15.7
Per-emb 35 B	NGC 1333 IRAS 1	03:28:37.22	31:13:31.74	7.3	Y20	0''66×0''42	0''78×0''53	0.75	86.8±20.6
Per-emb 27	NGC 1333 IRAS 2A	03:28:55.57	31:14:36.97	6.5	Y20	0''66×0''42	0''93×0''66	5.79	683.7±93.6
EDJ2009-172		03:28:56.65	31:18:35.43	0''66×0''42	0''69×0''44	0.62	196.4±20.0
Per-emb 36	NGC 1333 IRAS 2B	03:28:57.37	31:14:15.77	6.9	S19	0''66×0''42	0''73×0''46	5.56	666.5±93.4
Per-emb 54	NGC 1333 IRAS 6	03:29:01.55	31:20:20.49	7.9	S19	0''66×0''42	0''69×0''40	0.07	115.5±28.2
SVS 13B	NGC 1333 SVS 13B	03:29:03.08	31:15:51.73	8.5	S19	0''66×0''42	0''87×0''68	6.64	581.1±98.2
SVS 13A2	VLA 3	03:29:03.39	31:16:01.58	8.4	S18	0''66×0''42	0''86×0''53	0.61	102.6±27.7
Per-emb 44	NGC 1333 SVS 13A	03:29:03.76	31:16:03.70	8.7	S19	0''66×0''42	0''98×0''79	6.84	674.4±90.9
Per-emb 15		03:29:04.06	31:14:46.23	6.8	S19	0''66×0''42	0''89×0''70	0.17	<9.3±6.6
Per-emb 50	IRAS 03260+3111 A	03:29:07.77	31:21:57.11	9.3	Y20	0''66×0''42	0''73×0''44	4.13	535.2±91.0
Per-emb 12 B	NGC 1333 IRAS 4A2	03:29:10.44	31:13:32.08	6.9	S19	0''66×0''42	1''33×0''81	10.04	158.1±38.4
Per-emb 12 A	NGC 1333 IRAS 4A1	03:29:10.54	31:13:30.93	6.9	S19	0''66×0''42	1''11×0''98	21.85	2853.9±437.0
Per-emb 21	NGC 1333 IRAS 7 SM2	03:29:10.67	31:18:20.16	8.6	Y20	0''66×0''42	0''74×0''48	2.05	211.9±41.1
Per-emb 18	NGC 1333 IRAS 7 SM1	03:29:11.27	31:18:31.09	8.1	S19	0''66×0''42	0''84×0''73	3.42	224.8±47.1
Per-emb 13	NGC 1333 IRAS 4B1	03:29:12.02	31:13:07.99	7.1	S19	0''66×0''42	1''07×0''83	14.76	1271.3±207.6
IRAS4B'	NGC 1333 IRAS 4B2	03:29:12.85	31:13:06.87	7.1	S19	0''66×0''42	0''83×0''74	7.13	603.2±115.2
Per-emb 14	NGC 1333 IRAS 4C	03:29:13.55	31:13:58.12	7.9	S19	0''66×0''42	0''79×0''50	3.05	311.2±58.6
EDJ2009-235		03:29:18.26	31:23:19.73	7.7	Y20	0''67×0''42	0''66×0''44	0.26	16.6±10.0
EDJ2009-237		03:29:18.74	31:23:25.24	0''67×0''42	0''67×0''42	0.12	...
Per-emb 37		03:29:18.97	31:23:14.28	7.5	Y20	0''67×0''42	0''82×0''57	0.56	95.4±23.9
Per-emb 60		03:29:20.05	31:24:07.35	0''67×0''42	0''73×0''47	0.08	<13.3±8.1
Per-emb 5	IRAS 03282+3035	03:31:20.94	30:45:30.24	7.3	S19	0''45×0''30	0''56×0''41	15.29	502.3±86.3
Per-emb 2	IRAS 03292+3039	03:32:17.92	30:49:47.81	7.0	S19	0''45×0''30	1''35×0''97	7.41	927.4±175.6
Per-emb 10	B1-d	03:33:16.43	31:06:52.01	6.4	S19	0''46×0''30	0''49×0''32	1.82	143.4±30.7
Per-emb 40	B1-a	03:33:16.67	31:07:54.87	7.4	S19	0''46×0''30	0''47×0''32	1.44	72.9±18.0
Per-emb 29	B1-c	03:33:17.88	31:09:31.74	6.1	Y20	0''46×0''30	0''56×0''39	8.41	233.5±43.5
B1-b N		03:33:21.21	31:07:43.63	6.6	C16	0''46×0''30	0''56×0''47	7.67	483.8±85.1
B1-b S		03:33:21.36	31:07:26.34	6.6	C16	0''46×0''30	0''63×0''53	14.79	354.0±76.5
Per-emb 16		03:43:50.97	32:03:24.12	8.8	S19	0''50×0''32	0''61×0''52	0.35	<34.9±18.1
Per-emb 28		03:43:51.01	32:03:08.02	8.6	S19	0''50×0''32	0''56×0''32	1.52	23.5±16.6
Per-emb 1	HH 211 MMS	03:43:56.81	32:00:50.16	9.4	S19	0''49×0''32	0''68×0''48	4.57	279.6±50.0
Per-emb 11 B	IC 348 MMS	03:43:56.88	32:03:03.08	9.0	S19	0''50×0''33	0''92×0''69	0.40	21.7±14.9
Per-emb 11 A	IC 348 MMS	03:43:57.07	32:03:04.76	9.0	S19	0''50×0''33	0''61×0''48	10.47	413.5±73.1
Per-emb 11 C	IC 348 MMS	03:43:57.70	32:03:09.82	9.0	S19	0''50×0''33	1''10×0''86	0.34	30.5±15.4
Per-emb 55	IRAS 03415+3152	03:44:43.30	32:01:31.22	12.0	S19	0''50×0''32	0''49×0''33	0.32	56.1±12.9
Per-emb 8		03:44:43.98	32:01:35.19	11.0	S19	0''50×0''32	0''49×0''36	8.51	237.9±47.5
Per-emb 53	B5 IRS 1	03:47:41.59	32:51:43.62	10.2	Y20	0''51×0''33	0''58×0''42	1.55	56.6±22.6

References—C16=Carney et al. (2016); H18=Higuchi et al. (2018); S18=Stephens et al. (2018); S19=Stephens et al. (2019); Y20=this study.

^aThe dust mass is taken from Tychoniec et al. (2020).

NOTE—The dust masses for L1455 IRS 2, EDJ2009-235, EDJ2009-172 are taken from Tychoniec et al. (2018) by applying a gas-to-dust ratio of 100. The dust mass of unresolved multiple systems, such as L1448 NW, Per-emb 33 B/C, Per-emb 17, Per-emb 44, Per-emb 27, Per-emb 36, and Per-emb 55, are taken to be the total mass of multiple protostars. The dust mass of Per-emb 40 is assumed to be the dust mass of Per-emb 40 A as the dust mass of Per-emb 40 B is an upper limit.

six sources, Per-emb 33 A, NGC 1333 IRAS 4A2, NGC 1333 IRAS 4B1, Per-emb 5, B1-b S, and Per-emb 11 A, our observations detect several molecular lines from the central region, suggesting that the continuum opacity has less impact compared to that for IRAS 4A1. Previous observations also suggest less impact from the continuum opacity for NGC 1333 IRAS 4B1 (Belloche et al. 2020) and B1-b S (Marcelino et al. 2018). Most of the sources show averaged brightness temperatures lower than 10 K, suggesting that the continuum sources remain unresolved and have a negligible effect to the COMs emission. We take the T_b as a tracer of the averaged dust column densities. Constraining the actual column densities requires higher resolution observations.

3.2. Spectral Extraction

The ALMA image cubes are post-processed to extract 1D spectra for identifying the emission of complex molecules and further analyses. COMs typically desorb from dust grains at $T \gtrsim 100$ K, which coincidentally corresponds to ~ 100 au for typical embedded protostars (e.g., Yang et al. 2020). Given the spatial resolution of $\sim 0''.5$ (~ 150 au), we focus on the spectra toward the continuum sources to search for the COMs in the inner envelope. In most of the cases, COMs emission concentrates around the protostars at $\lesssim 300$ au scale. Figure 2 shows representative sample of the COMs emission, while the maps for the entire sample are shown in Appendix C. Three steps of post-processing reduces the image cubes to 1D spectra, which are summarized below.

- Extracting spectra: We use the CASA task `specflux` to extract the mean flux density within the ellipse which has the same major and minor axes as well as the position angle as the fitted continuum sources.
- Baseline calibration: The continuum has been removed before the imaging process; however, the extracted spectra sometimes still show imperfect baselines due to rich emission lines, lack of emission, and broad features. Thus, we manually select the frequency ranges for baseline calibration for each spectral window and each field.
- Velocity correction: Finally, the frequency of the extracted spectra are corrected according to the source velocities. We collect the source velocities from the literature as well as from the strong emission lines in our spectra, such as SO and CS. Table 3 lists the adopted source velocities and the corresponding references.

3.3. Line Identification and Modeling

Line identification starts with manual identification and verification for a few sources with rich spectra, including Per-emb-12B and B1-bS. We use SPLATALOGUE¹ to identify the molecular species and use XCLASS (Möller et al. 2017) to verify the identification. The XCLASS package is a LTE radiative transfer code that uses the molecular data from the Cologne Database of Molecular Spectroscopy (CDMS; Müller et al. 2001, 2005; Endres et al. 2016) and the Jet Propulsion Laboratory (JPL; Pickett et al. 1998). An identification needs to satisfy the following criteria.

- The spectra agree with the predicted strengths of the model.
- The spectral lines are not all blended with other emission, such as other molecules and the SiO emission tracing the outflows. The emission of a few species, such as HDCO & $^{13}\text{CH}_3\text{OH}$, CH_3OH & HCOOCH₃, CH₃CHO & CH₂DOH, ^{34}SO & C₂H₅OH, and CH₃OCH₃ & CH₂DCN, are partially blended (blending occurs at a few lines but other lines remain isolated). The fittings of those species are performed together to verify their identification.
- Identified molecules need to be already found toward young stellar objects as summarized in McGuire (2018).

Table ?? lists the identified species and transitions that are detected in at least one of the PEACHES protostars. Only identifiable transitions are listed. The XCLASS modeling include all the transitions in our frequency coverage for each molecule regardless their Einstein-A values and upper energy levels.

As shown in Figure 2, COMs emission centers around the protostars at $\sim 100 - 200$ au. At the similar region, the gas density is around $\sim 10^8 \text{ cm}^{-3}$ (B1-b S: Gerin et al. 2017), similar to the critical density of the COM emission detected in our observations. For example, the CH₃OH line at 243915 MHz has a critical density of $1.4 \times 10^8 \text{ cm}^{-3}$ (Schöier et al. 2005; Rabli & Flower 2010). Thus, the assumption of LTE holds for modeling the COM emission. **YLY: B1-b S is one of the most dense protostars. My guess is that the COMs is close to LTE but not in LTE. We also test the LTE assumption on CH₃OH with the large velocity gradient (LVG) model using RADEX (reference). The column density difference is only X%.**

¹ <http://www.splatalogue.net/>

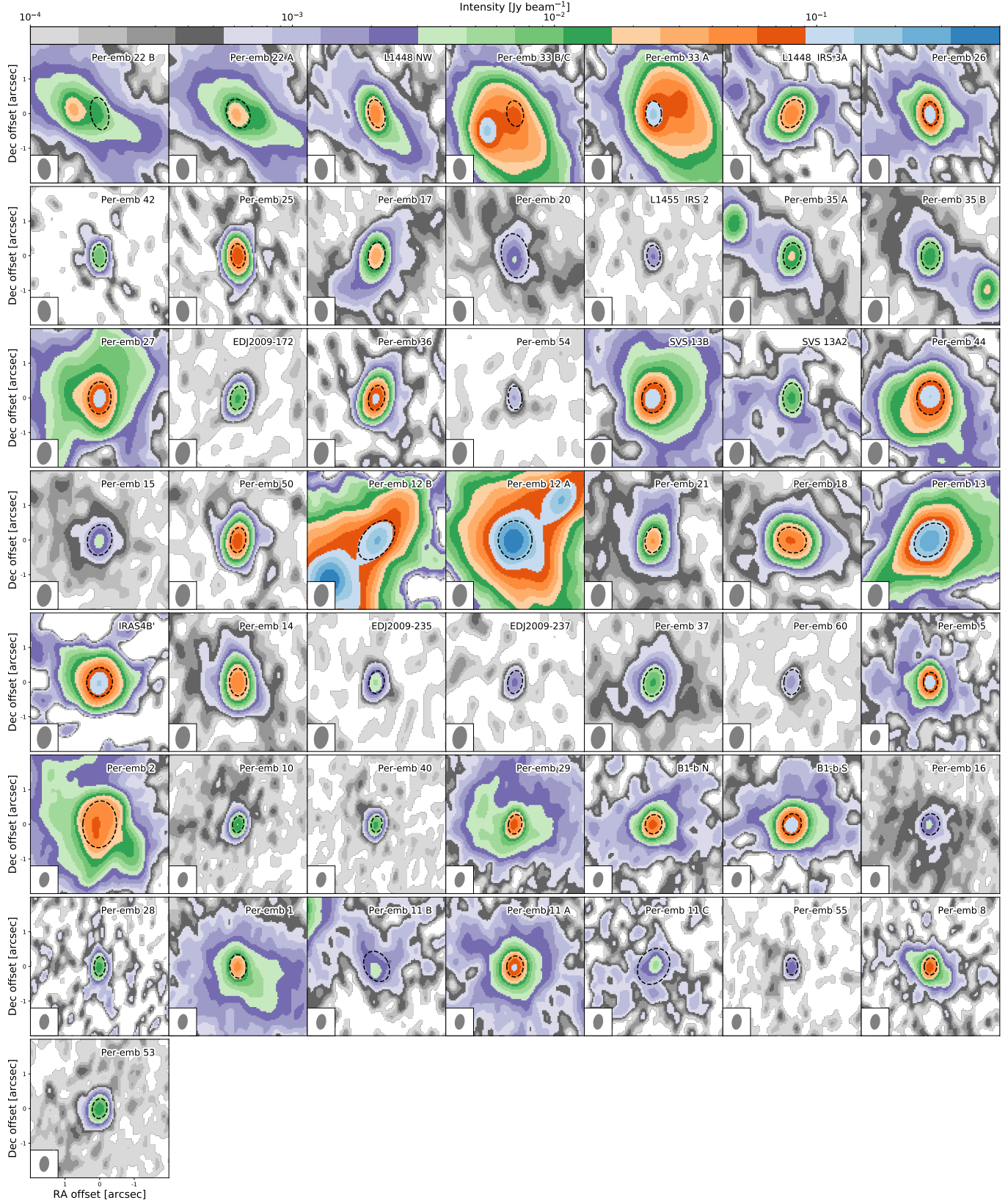


Figure 1. The continuum images of all PEACHES protostars. Non-detections toward L1448 IRS 2E and NGC 1333 SVS 3 are not shown. The dashed ellipses illustrate the size of fitted continuum, which is the region for extracting 1D spectra.

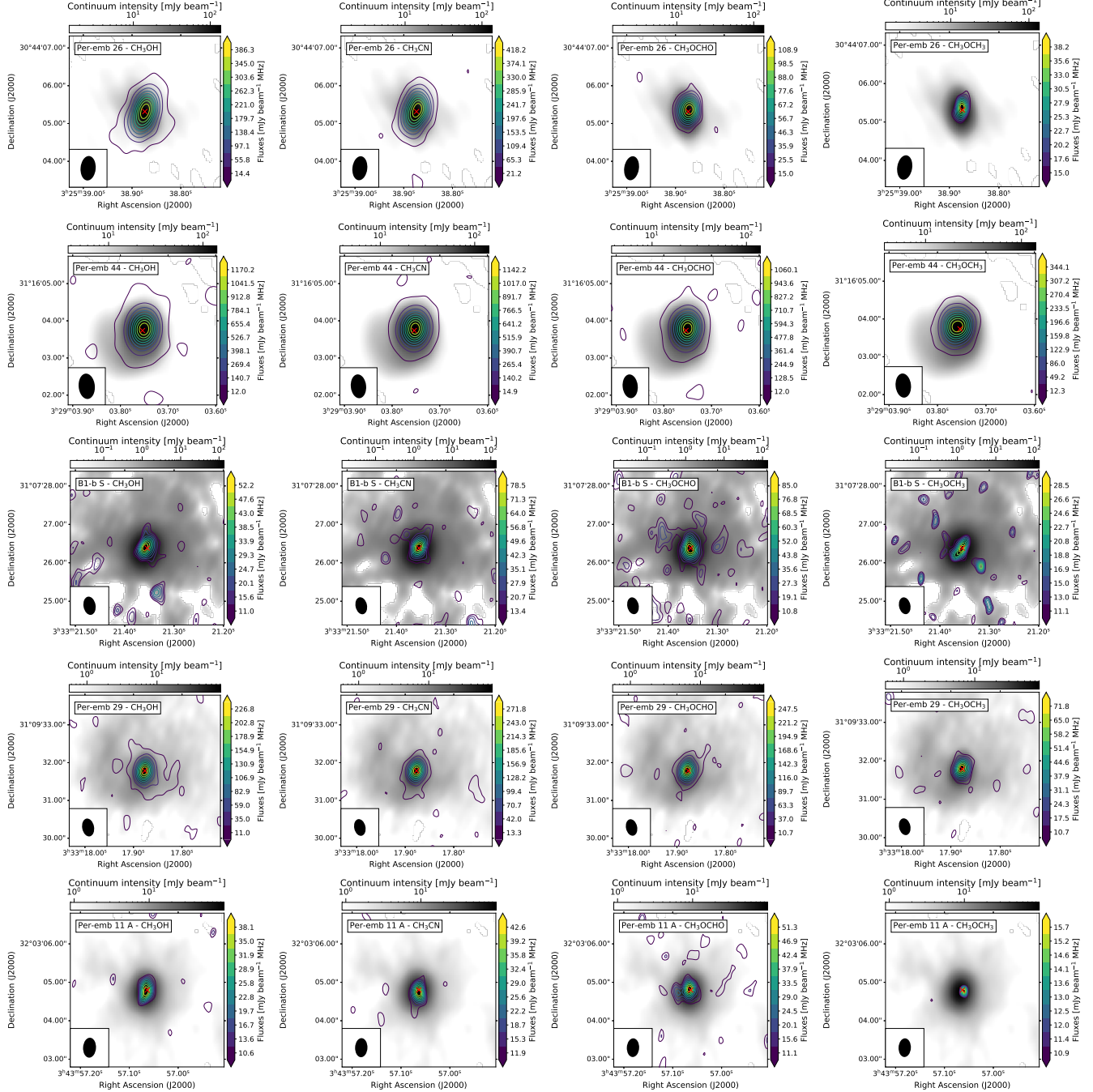


Figure 2. The intensity maps of most detected COMs, CH₃OH, CH₃CN, HCOOCH₃, and CH₃OCH₃ (from left to right). Each row shows the emission from Per-emb 26, Per-emb 44, B1-b S, B1-c, and Per-emb 11 A (top to bottom). The intensity is calculated by integrating over 3 km s⁻¹ around the line centroid, while the lowest contour shows the 3σ value. The grayscale images illustrate the continuum emission.

Systematic spectral fitting using xCLASS is applied to all sources using a list of species, compiled from the identifications. Appendix A lists the catalogs used in this study. The fitting function in xCLASS includes several optimization algorithms that can be used in series to reduce biases. We configure the algorithm chain that starts with the genetic algorithm followed by the Levenberg-Marquardt χ^2 minimization. The genetic algorithm searches the best-fitting parameters iteratively with generations that evolve like a natural selection, where the better fitting models get less modification over generations. We setup the genetic algorithm to search for the top two best-fitting models with 30 generations. Then, the Levenberg-Marquardt χ^2 minimization applies to the two best-fitting models for 20 iterations to find the best-fitting models. The genetic algorithm aims to find local minimums and the Levenberg-Marquardt minimization further finds the best-fitting models in the local minimums. The two best-fitting models found by the genetic algorithm often very similar, suggesting that there is only one minimum. To address the rare cases of two separated local minimums, we pick the model with the lower χ^2 values from the two best-fitting models constrained by the Levenberg-Marquardt minimization.

There are five parameters in the xCLASS modeling, the size of the emitting molecule (r_{COM}), the excitation temperature (T_{ex}), the column density (N_{COM}), the line width ($\Delta\nu$), and velocity offset (v_{off}). We assume the COMs are all concentrated at the center, simplified as a 2D thin circular disk. We fix r_{COM} as $0''.5$, similar to our beam size, and optimize the model with five excitation temperatures, 100, 150, 200, 250, and 300 K. We allow the line width varying between 1.2 km s^{-1} to 3.5 km s^{-1} for better fitting quality but assume no velocity offset from the source velocity, and the allowed range of the column density for each molecule is chosen according to the strength of the emission. From the fitting results of five T_{ex} , if a molecule is detected, the mean column densities will be the best-fitting column density, while the range of the column densities indicates the upper and lower uncertainties. If a molecule is non-detection, the synthetic spectra for all lines are scaled to match the peaks of the each line fitted by a Gaussian profile. Then, we take the minimum of the corresponding column densities as the upper limit.

4. RESULTS

4.1. Detection Statistics

We summarize the detection statistics in Figure 3, which includes COMs, the carbon-chain molecules, and the simple organic molecules, such as CS, H^{13}CN , SO, ^{34}SO , and SO_2 . In the following results of detection

fraction, we include the three sources that are excluded from modeling due to no reliable source velocity, making a total of 50 sources. The COMs discussed here are the derived from the spectra taken toward the continuum peak (Section 3.1). We focus on the chemistry of COMs in the disk-forming regions in this study, therefore, excluding detection of molecules outside the continuum peak. A comparison of chemical composition in protostellar envelopes (100–1000 au) requires observations with larger maximum recoverable scale (θ_{MRS}).

The PEACHES protostars show a great chemical diversity from no molecule detected (e.g., B1-b N and L1455 IRS 2) to rich spectra of COMs (e.g., Per-emb 13). Most of the PEACHES protostars have simple organics, such as SO, CS, H^{13}CN , and HDCO, and $\sim 60\%$ of sources have SO_2 and ^{34}SO . Emission of C_2H can be easily identified from the spectra. However, the C_2H toward the continuum sources often shows irregular line profiles together with velocity offsets and absorption (Figure 16). In fact, warm environments, such as the outflow cavity wall, easily enhance the abundance of C_2H because of elevated abundance of C^+ (e.g., Zhang et al. 2018; Imai et al. 2019). Thus, C_2H emission is extended along with the outflow cavities, making the 1D spectra toward the continuum source unrepresentative. Observations with a larger θ_{MRS} will provide a complete representation of the C_2H abundance on the inner envelope.

Several sources have their SiO emission with a broad line width, significantly contaminating the emission of $\text{CH}_3\text{CH}_2\text{CN}$ and CH_3CHO . In the later quantitative discussion, we exclude the spectral windows contaminated by the SiO emission. For assigning the detections, we can distinguish the emission of $\text{CH}_3\text{CH}_2\text{CN}$ and CH_3CHO from the broad SiO emission in a few sources, such as CH_3CHO in Per-emb 26.

Figure 4 shows the number of COMs detected toward the PEACHES sample. Twenty-one (45%) sources have no COMs detected. CH_3OH is detected in 28 sources (56%); HCOOCH_3 is detected in 15 sources (32%); and N-bearing COMs are detected in 20 sources (40%). Comparing to the COMs in the CALYPSO survey (Belloche et al. 2020), the fraction of sources that have methanol, $\sim 50\%$, is similar to that for the PEACHES protostars. Also, 30% of the CALYPSO sources have at least three COMs, while 28% of the PEACHES protostars have at least three COMs.

We compare the number of detected COMs with the bolometric luminosity (L_{bol}), the bolometric temperature (T_{bol}), and the dust mass estimated by Tychoniec et al. (2020) using observations at 9 mm (M_{central}). The number of COMs shows no obvious trend with L_{bol} ,

T_{bol} , and M_{central} . For L_{bol} , the sources with at least three COMs all have $L_{\text{bol}} \gtrsim 3 M_{\odot}$, except for B1-b S. However, the sources without any COMs also have a similar L_{bol} . If COMs mostly come from thermal desorption, the region with $T > T_{\text{desorption}}$ may be smaller for the low luminosity sources, making the emission of COMs fainter and reducing our sensitivity to detect COMs. The COM-rich sources have $T_{\text{bol}} \sim 50$ K, while the COM-poor sources have a greater scatter of T_{bol} , ranging from 14.7 K to 1100 K. The protostars with high M_{central} ($> 666.5 M_{\oplus}$) have detections of COMs. However, the protostars with low M_{central} can have either many COMs or no COM.

The sources with high continuum brightness temperature ($T_{\text{b,cont}}$) tend to have rich spectra COMs (Figure 5), while the sources with no detection of COM have their $T_{\text{b,cont}} \lesssim 10$ K. The brightest source in continuum, Per-emb 12 A has many molecules detected in absorption due to the high continuum opacity blocking the emission of COMs (Sahu et al. 2019; De Simone et al. 2020). The continuum brightness temperature traces the gas column density, tracing the amount of embedding gas around the protostars. Thus, the tendency between many COMs and the high $T_{\text{b,cont}}$ hints the scenarios where the denser envelope either increases the detectability of COMs or enhance the complexity of molecules.

Compact emission of COMs (~ 100 – 300 au) suggests a warm temperature ($\gtrsim 100$ K) of COMs for a typical low-mass protostars (e.g. Yang et al. 2017), consistent with an origin of thermal desorption at the inner envelope, so called hot corinos (Ceccarelli 2004). Only L1448 IRS 3A shows extended CH₃OH emission, and B1-b N shows no CH₃OH emission toward the continuum but peaks at $\sim 1''$ away from the continuum, hinting the existence of CH₃OH toward the continuum source blocked by opaque continuum (Marcelino et al. 2018). Excluding L1448 IRS 3A, 28 sources (56%) have hot corinos type chemistry. Many of hot corinos are previously known (reference?), while our survey detects COMs other than CH₃OH toward Per-emb 35 A, Per-emb 35 B, Per-emb 11 A, Per-emb 11 C, and HH 211 MMS.

4.2. Column Densities

4.2.1. Excitation Temperatures

The PEACHES spectra cover four methanol lines, while the spectra of each source include three of them due to the frequency shift in the wide spectral window. The three methanol lines have upper energy ranging from ~ 50 K to ~ 500 K, which allows us to estimate the rotational temperature of methanol if all three lines are detected. To construct the methanol rotational di-

Table 4. Rotational Temperatures of Methanol

Source	T_{rot}
Per-emb 26	$120.1^{+2.6}_{-2.5}$ K
Per-emb 22 A	$182.4^{+11.2}_{-11.4}$ K
Per-emb 22 B	$157.5^{+13.4}_{-13.0}$ K
Per-emb 17	$173.9^{+1.8}_{-1.9}$ K
Per-emb 44	$197.5^{+0.3}_{-0.3}$ K
Per-emb 12 B	$194.0^{+0.8}_{-0.8}$ K
Per-emb 13	$208.6^{+3.9}_{-4.0}$ K
Per-emb 27	$195.8^{+0.4}_{-0.4}$ K
Per-emb 21	$151.0^{+14.6}_{-15.6}$ K
Per-emb 35 A	$145.1^{+3.7}_{-3.7}$ K
Per-emb 18	$395.7^{+30.7}_{-30.4}$ K
B1-bS	$241.7^{+11.7}_{-11.9}$ K
Per-emb 29	$227.7^{+3.2}_{-3.3}$ K

agram, we fit the methanol emission with a Gaussian profile and bootstrap the measurements for fitting the rotational temperature. Figure 6 shows the rotational diagram of Per-emb 22 B along with the sampled rotational temperature. The derived rotational temperature of methanol ranges from 120 K to 240 K with an exception of Per-emb 18, which has a rotational temperature of 395.7 K for methanol (Table 4).

YLY: need to redo the MCMC fitting. The fitting shown here is ~ 6 months old. For the sources with significant emission of HCOOCH₃, the column density and the excitation temperature of HCOOCH₃ can be constrained with MCMC. Table 5 lists the sources where the MCMC fitting is feasible and the derived properties of HCOOCH₃. The best-fitting temperatures range from 100–300 K with a few outliers at ~ 1000 K. The spectra with the high excitation temperature show non-Gaussian line profiles, making the fitting inaccurate. Therefore, we exclude those sources in Table 5.

[put the derived values from HCOOCH₃ for several sources, and say consistency with several other works.] [Put the discussions in 6.1.1. in your section number, and say consistency with HCOOCH₃. [say the assumption/justification of T for sources without multiple line detections(i.e. sources, which is difficult to derive T). It could partly be overlapped with the section 3.2 (3.1 in your numbering)]]

4.3. Correlations of COMs

The chemical evolution of protostars may leave certain patterns in the abundance of molecules as the dynamical evolution determines the density and temperature structures, which regulate chemical reactions. Thus, the abundance of COMs and their correlations provide crit-

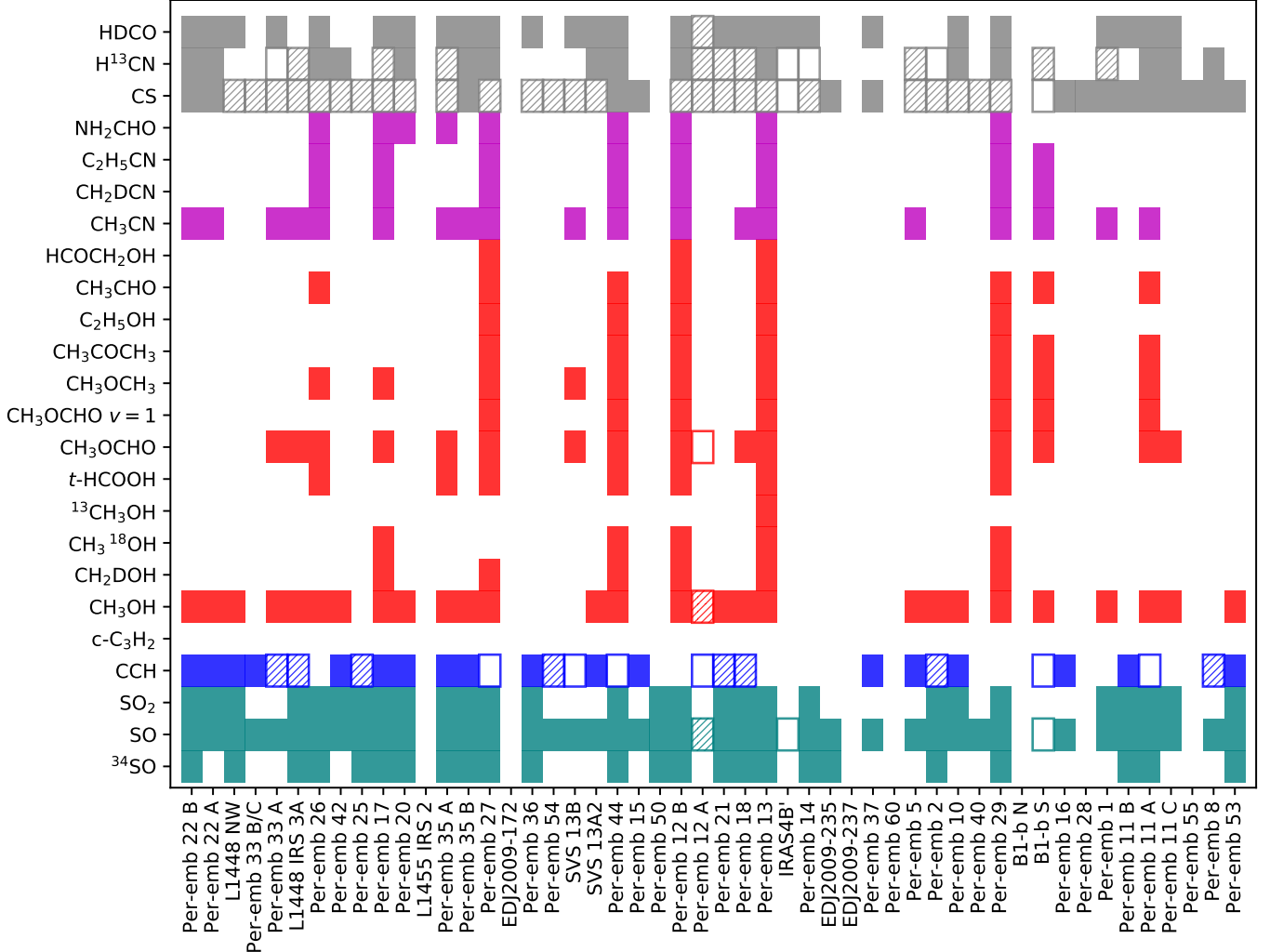


Figure 3. Summary of molecular detections. The sources are sorted by increasing R.A. from left to right. The detections are color-coded by the types of species: S-bearing molecules in green, carbon-chain molecules in blue, O-bearing COMs in red excluding N-bearing molecules, N-bearing COMs in magenta, other simple organics in gray. The boxes with solid colors indicate emission and the empty boxes indicate absorption. The hatched boxes indicate both emission and absorption are seen.

ical information to constrain the chemical evolution at embedded protostars.

As described in Section 3.3, we fit the column density and line width with different excitation temperatures, resulting in a range of column density as its uncertainty. To quantify the goodness of correlation, we calculate the Pearson’s correlation coefficient (r), which tests the linearity of two variables. A simple calculation of the Pearson’s correlation coefficient would ignore the uncertainties of the column density. Thus, we use the bootstrapping method to sample the fitted column densities to calculate Pearson’s r , by assuming a normal distribution centers on the best-fitted values with the uncertainty as the width of the normal distribution. If we include the upper limits as normal distributions center on zero, the correlation coefficient becomes significantly

lower due to the cluster of samples around zero column density (Figure 8). With the detection-only sample, the mean Pearson’s r_d is 0.91, as expected for a tight correlation, with a Gaussian-like distribution skewed toward lower values. After including the upper limits, the mean Pearson’s r decreases to 0.59 with larger uncertainty (the 68% credible interval increases by 160%). Thus, the bootstrapped correlation coefficient only considers the detections.

Figure 9 shows the correlations of several COMs selected from their detection rates as well as the ratios between species which is discussed in Section 5.2. The column density of CH₃OH best correlates with that of CH₃CN. Belloche et al. (2020) also found the tight correlation between these two molecules from the CALYPSO survey, which has a selective sample. The

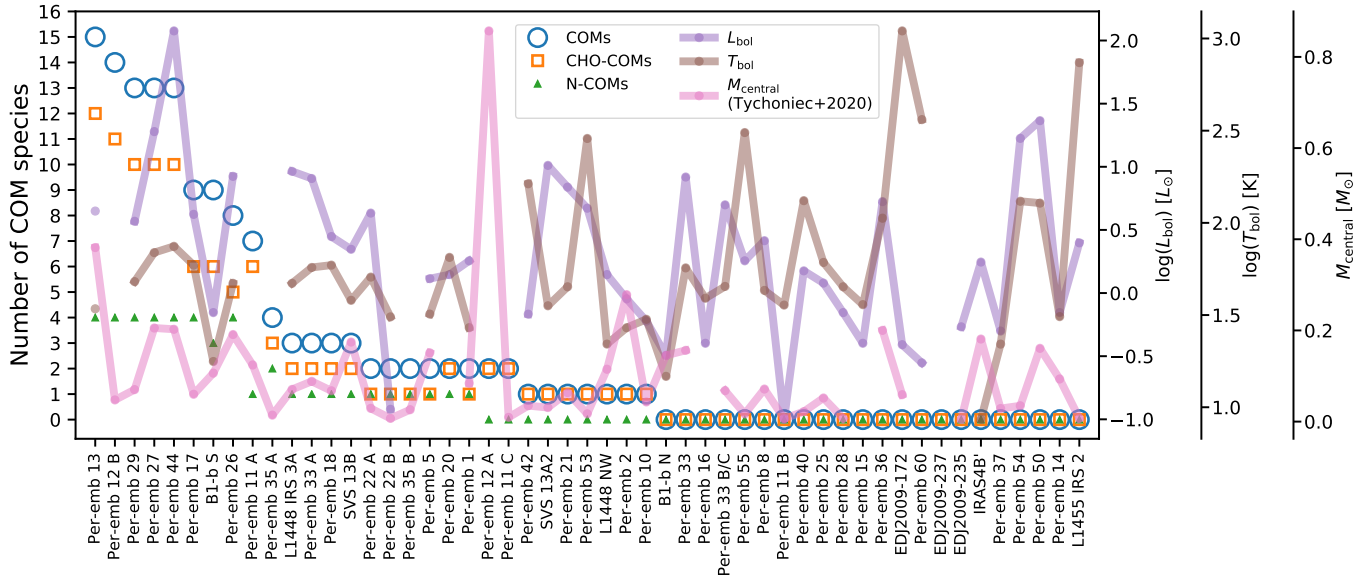


Figure 4. The number of COMs detected toward the PEACHES sources compared with the bolometric luminosity (purple), the bolometric temperature (brown), and the central dust mass (pink, Tychoniec et al. (2020)). The sources are sorted by the total number of COMs with the number of O-bearing COMs, N-bearing COMs, and all COMs labeled as orange boxes, green triangles, and blue circles, respectively. The mass of unresolved systems is estimated as the sum of each protostar. The bolometric luminosities and the bolometric temperatures are taken from Tobin et al. (2016) and Murillo et al. (2016).

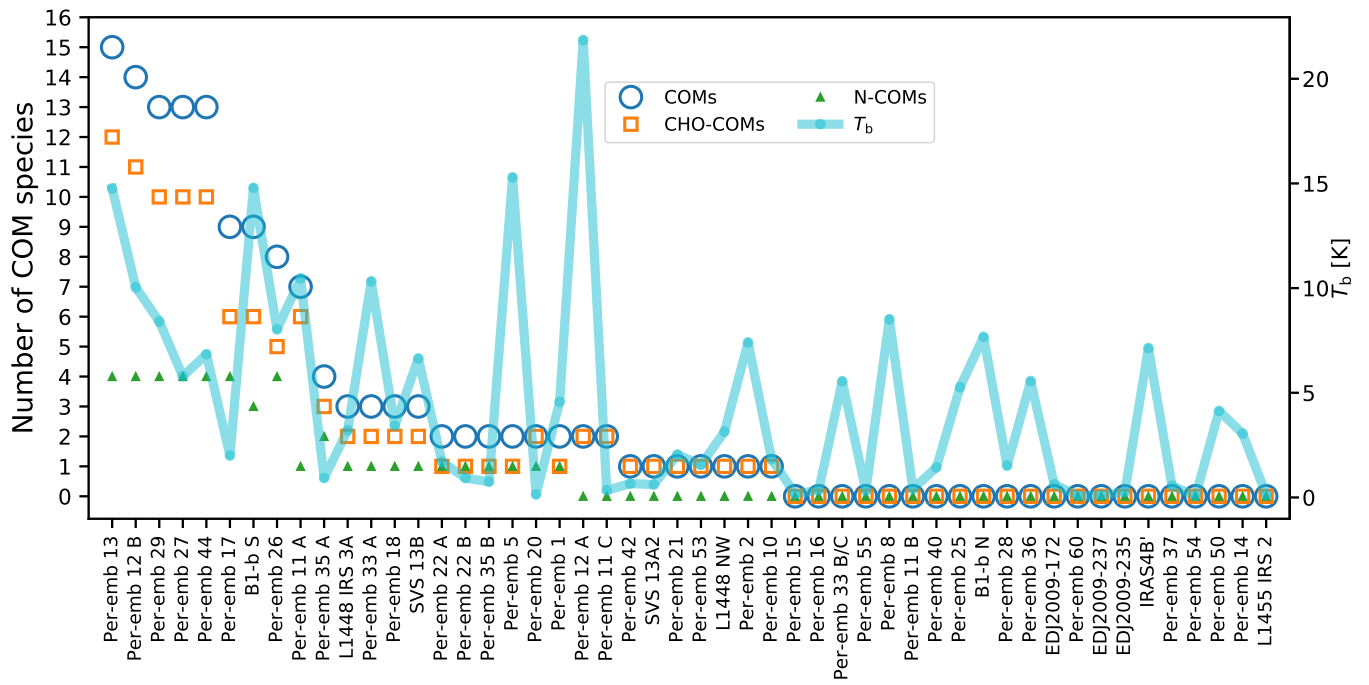


Figure 5. The number of COMs detected toward the PEACHES sources compared with the continuum brightness temperature. The legends for the protostars are the same as Figure 4. The brightness temperatures are indicated in green.

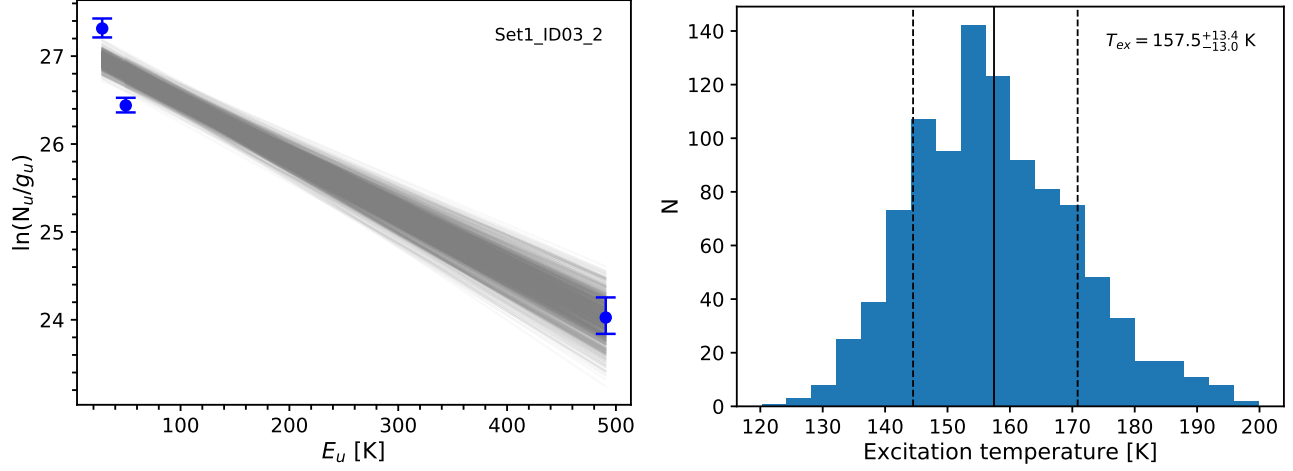


Figure 6. The methanol rotational diagram for Per-emb 22B and the fitted excitation temperature distribution using the bootstrapping method.

Table 5. MCMC Fitting of Methyl Formate

Source	Temperature [K]		$\log(\mathcal{N})$ [cm^{-2}]		Line width [km s^{-1}]	
	best	mode \pm HPD	best	mode \pm HPD	best	mode \pm HPD
Set1_ID01_2	95	76^{+315}_{-56}	15.24	$15.29^{+0.42}_{-0.42}$	4.86	$4.77^{+0.22}_{-0.52}$
Set1_ID02	87	98^{+14}_{-41}	15.67	$15.67^{+0.10}_{-0.08}$	3.66	$4.06^{+0.65}_{-0.79}$
Set1_ID06	93	93^{+59}_{-35}	15.67	$15.67^{+0.12}_{-0.08}$	4.84	$4.77^{+0.22}_{-0.02}$
Set2_ID00	263	310^{+3}_{-56}	16.89	$16.92^{+0.05}_{-0.04}$	3.95	$3.95^{+0.15}_{-0.12}$
Set2_ID01_2	217	194^{+75}_{-4}	16.37	$16.36^{+0.10}_{-0.03}$	2.22	$2.25^{+0.14}_{-0.12}$
Set2_ID02	195	225^{+119}_{-64}	16.04	$16.10^{+0.20}_{-0.09}$	1.21	$1.21^{+0.00}_{-0.01}$
Set2_ID07	152	131^{+281}_{-120}	14.79	$14.72^{+0.53}_{-0.43}$	3.24	$1.66^{+2.26}_{-0.40}$
Set2_ID08	159	10^{+551}_{-0}	14.75	$14.11^{+0.85}_{-0.04}$	2.37	$1.20^{+2.15}_{-0.00}$
Set2_ID12	115	41^{+269}_{-30}	14.96	$15.02^{+0.05}_{-0.94}$	4.54	$4.89^{+0.09}_{-1.70}$
Set3_ID00	98	58^{+41}_{-14}	15.85	$15.82^{+0.26}_{-0.09}$	1.24	$1.25^{+0.02}_{-0.05}$
Set3_ID01	134	134^{+13}_{-27}	16.59	$16.60^{+0.02}_{-0.02}$	3.04	$3.08^{+0.18}_{-0.15}$
Set3_ID07	104	92^{+182}_{-45}	15.67	$15.67^{+0.29}_{-0.15}$	2.44	$2.33^{+1.22}_{-0.66}$

column densities of CH_3OCH_3 and HCOOCH_3 also show a tight correlation. CH_3OH also correlates with more complex species (i.e. so called daughter species, HCOOCH_3 and CH_3OCH_3) with a lower correlation coefficient than that between CH_3OH and CH_3CN . The correlations between CH_3CN and more complex species also show the same behavior. The decreasing strength of correlation with between the simple COMs and more complex COMs supports the hypothesis that CH_3OH and CH_3CN are first generation species and HCOOCH_3 and CH_3OCH_3 are the second generation (reference). The correlations of CH_3OH , CH_3CN , HCOOCH_3 , and CH_3OCH_3 with other COMs show positive trends; however, the correlations are driven by a few sources due to the low detection rate of other COMs (Figure 11).

The column densities shown in Figure 9 and 11 are the column densities within a $0''.5$ region. The correlations remain similar for the column densities averaged within the extracted region. To directly compare the abundance of COMs, we normalize the column densities of COMs by the $T_{\text{b,cont}}$, which is a proxy of gas column density. The normalized column densities of COMs show similar correlations as that of the column densities (Figure 10). We further normalize the “abundance” of COMs ($N_{\text{COM}}/T_{\text{b}}$) with L_{bol} and T_{bol} to test the effect of the protostellar evolutionary stage on the observed complex chemistry (Figure 10, green and orange). After the normalization with L_{bol} and T_{bol} , the correlation coefficients remain similar for most cases. Normalized with L_{bol} and T_{bol} , the correlation between CH_3OH and CH_3OCH_3 decreases significantly, while CH_3CN shows a moderate decrease of correlation with CH_3OCH_3 . However, the correlations between HCOOCH_3 and CH_3OCH_3 remain similar with different normalizations. The column densities correlations of $\text{CH}_3\text{OH} \& \text{CH}_3\text{OCH}_3$ and $\text{CH}_3\text{CN} \& \text{CH}_3\text{OCH}_3$ are also lower than that of other combinations of species. Thus, the evolutionary stage of protostars plays an insignificant role on determining the abundance of most COMs but has a substantial effect for CH_3OCH_3 .

5. DISCUSSION

5.1. Universal Chemistry among Hot Corinos?

For the protostars with compact emission of COMs, so called hot corinos, the abundance of COMs correlates well between species. With the normalization of $T_{\text{b,cont}}$, the Pearson’s r for the correlations between the four major species (CH_3OH , CH_3CN , HCOOCH_3 , and CH_3OCH_3) are 0.76–0.93 (Figure 10). The Pearson’s r for the four major species with all COM species has a median value of 0.86 with a range from 0.57 to 0.95 (Figure 11). The correlations remain strong with the normal-

izations of L_{bol} and T_{bol} , suggesting that the chemistry of COMs may be independent of the evolutionary stage of protostars. The limited number of detections for the four major COMs with all COMs prohibits us to further quantify their correlation strengths.

We further test the effect of protostellar evolution with the abundance ratios of the four major COMs (Figure 12). The ratios of $\text{CH}_3\text{CN}/\text{CH}_3\text{OH}$ and $\text{CH}_3\text{OCH}_3/\text{HCOOCH}_3$, which are molecules with a similar complexity, have little variation as the functions of L_{bol} , T_{bol} , and $T_{\text{b,cont}}$. In contrast, the ratios of $\text{HCOOCH}_3/\text{CH}_3\text{OH}$ and $\text{CH}_3\text{OCH}_3/\text{CH}_3\text{OH}$, which are molecules with different complexity, increases with $T_{\text{b,cont}}$, whereas the ratios show tentatively decreases with L_{bol} and T_{bol} . Because of its high abundance, methanol may be more optical thick at a higher gas column density (high $T_{\text{b,cont}}$), resulting in an underestimation of methanol column density, hence the elevated ratios. The emission of CH_3CN is likely to be optical thin given its low abundance compared to that of CH_3OH . Therefore, the insignificant trend in ratios of $\text{CH}_3\text{CN}/\text{CH}_3\text{OH}$ with $T_{\text{b,cont}}$ indicates a negligible role of optical depth. Chemical evolution is an alternative scenario for such trend. Under the scheme of grain-surface chemistry, CH_3OH primarily forms from the hydrogenation of CH_3O or CH_2OH , while HCOOCH_3 primarily forms from the reaction of HCO and CH_3O and CH_3OCH_3 primarily forms from the reaction of CH_3 and CH_3O (Garrod et al. 2008). Thus, the elevated ratios of HCOOCH_3 and CH_3OCH_3 to CH_3OH hint a higher abundance of HCO and CH_3 at high $T_{\text{b,cont}}$ sources for more efficient formation of HCOOCH_3 .

size of COMs vs. Lbol

No tight correlation with physical parameters. –
hot corino emergence would not be the “determined story” in chemical evolution. [refer figures 3/4] [add some discussions of the position of hot corino sources]

5.2. The Abundance Ratios of O-bearing and N-bearing COMs

- [please mention about abundance ratios $\text{C}_2\text{H}_5\text{CN}$, NH_3CHO vs CH_3OCH_3 and CH_3OCHO . and refer several papers discussed the O- and N difference. such as in Orion KL and/or IRAS16293???]
O- and N- difference might be enhanced in more complex species (?).

5.3. Origin of the $\text{CH}_3\text{OH}/\text{CH}_3\text{CN}$ Correlation

The tight correlation between CH_3OH and CH_3CN is a striking finding of the PEACHES survey, while studies such as Bergner et al. (2017); Belloche et al. (2020) have shown a similar trend with fewer detections or larger scatter. Belloche et al. (2020) argue that this correlation between CH_3OH and CH_3CN may not be due to

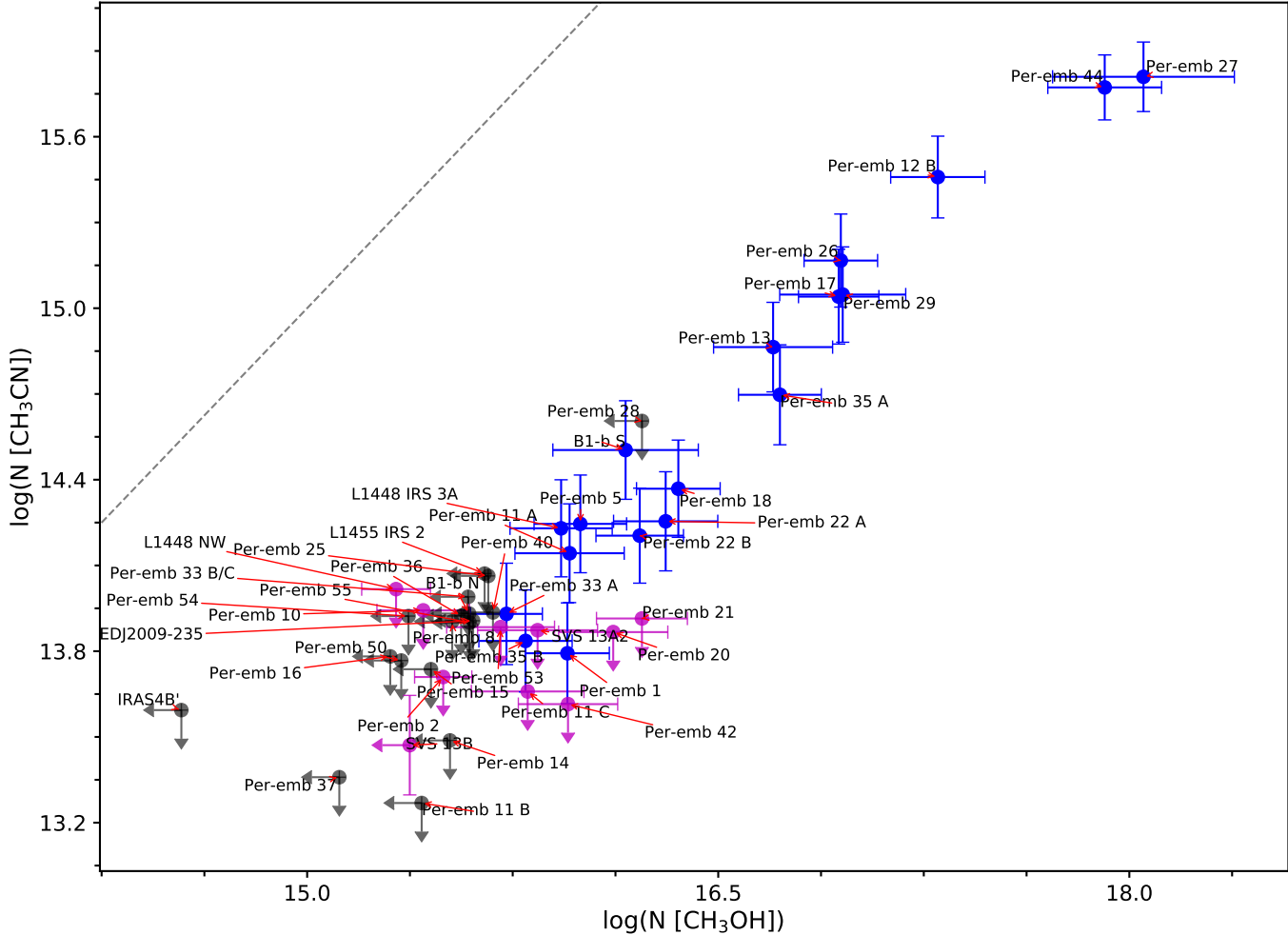
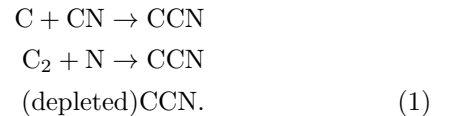


Figure 7. Correlation of the fitted column densities of CH₃OH and CH₃CN from the PEACHES protostars. The sources where both molecules are detected are shown in black; the sources where only one molecule is detected are shown in magenta; finally, the sources where both molecules are not detected are shown in black for the corresponding upper limits.

chemistry because of the somewhat unrelated formation pathways of two molecules. If the gas-phase chemistry is negligible for the production of CH₃OH and CH₃CN, the tight correlation between CH₃OH and CH₃CN suggests a similar abundance ratio of two molecules on the icy grains prior to being thermally desorbed. Thus, the chemical processes that produce these two molecules may occur at a much shorter timescale compared to the dynamical scale of the protostellar evolution, hinting a universal chemistry of COMs at the warm protostellar envelope. The tight correlation may also reflect a uniform elemental abundance of O and N in the Perseus molecular cloud before the star formation.

The compact emission of CH₃OH has a well known icy origin, where CH₃OH forms via the hydrogenation on the surface of dust grains. At cold temperature, the non-thermal desorption is thought to responsible for the production of CH₃OH. CH₃CN can also form in gas-phase via radiative association (HCN + CH₃⁺ →

$\text{CH}_3\text{CNH}^+ + h\nu$) followed by the dissociative recombination of CH_3CNH^+ or on the grain surface. The grain-surface reactions to form CH_3CN can occur at cold temperature by the hydrogenation of CCN, which can form via



At warm temperature, CH₃CN can form directly from reactions between radicals, CH₃ and CN. For embedded protostars, the grain-surface reactions are thought to dominate the production of CH₃CN; however, it remains unclear whether the cold phase or warm phase grain-surface pathway regulates the abundance of CH₃CN.

If we assume an icy grain origin for both CH₃OH and CH₃CN, we can test the efficiency of the cold and warm phase pathways by comparing the ratio of

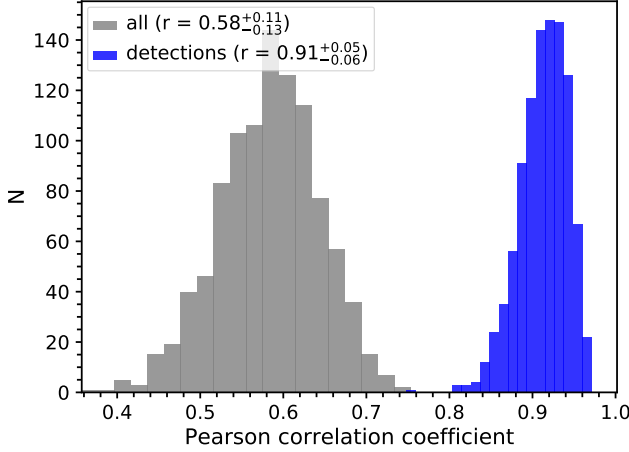


Figure 8. Distributions of Pearson’s correlation coefficient from 10000 resamples drawn from detections + non-detections and only detections. The legend indicates the mean values of Pearson’s r along with the range of the 95% credible interval as the associated uncertainties.

CH3CN/CH3OH toward the prestellar and protostellar sources. **YLY:** methanol must be released from dust grains via non-thermal reactions. I recall there are some chemical reactions that can form methanol other than the grain-surface chemistry, perhaps some form of gas-phase chemistry, but don’t know for sure now. At prestellar cores, [CH3CN/CH3OH] are 0.28, 0.039, and 0.042 for TMC1 (Gratier et al. 2016), L1521 E (Nagy et al. 2019), and L1544 (Nagy et al. 2019), re-

spectively, all of which are higher than the ratio in our survey, $0.012^{0.009}_{0.005}$. The decreases of [CH3CN/CH3OH] from prestellar to protostellar phase suggests that the warm phase grain-surface chemistry plays a rather insignificant role for the production of CH3CN and/or the gas-phase chemistry is more efficient at the cold phase to produce additional CH3CN.

6. CONCLUSION

Y.-L. Yang acknowledges the supports the JSPS Postdoctoral Fellowship from Japan Society for the Promotion of Science. This paper makes use of the following ALMA data: ADS/JAO.ALMA#2016.0.00391.S. ALMA is a partnership of ESO (representing its member states), NSF (USA) and NINS (Japan), together with NRC (Canada), MOST and ASIAA (Taiwan), and KASI (Republic of Korea), in cooperation with the Republic of Chile. The Joint ALMA Observatory is operated by ESO, AUI/NRAO and NAOJ. The National Radio Astronomy Observatory is a facility of the National Science Foundation operated under cooperative agreement by Associated Universities, Inc.

Facilities: ALMA

Software: astropy (Astropy Collaboration et al. 2018), XCLASS (Möller et al. 2017), spectral-cube (Robitaille et al. 2016), CASA (McMullin et al. 2007)

APPENDIX

A. CATALOGS FOR MOLECULAR DATA

The spectroscopic data are taken from the Cologne Database of Molecular Spectroscopy (CDMS; Müller et al. 2001, 2005; Endres et al. 2016) and the Jet Propulsion Laboratory (JPL; Pickett et al. 1998). Here we list only the references that cover the frequencies relevant to this study.

For CH3OH, the data were taken from Xu et al. (2008); for CH2DOH, the data were taken from Pearson et al. (2012); for ^{13}CH3OH, the data were taken from Xu & Lovas (1997). For HCOOCH3, the data were taken from Ilyushin et al. (2009), which includes the data from Plummer et al. (1984); Oesterling et al. (1999); Carvajal et al. (2007); Maeda et al. (2008). For CH3CHO, the data were taken from Kleiner et al. (1996). For CH3OCH3, the data were taken from Endres et al. (2009). For CH3COCH3, the data were taken from Groner et al. (2002). For CH3C^{15}N, the data were taken from Müller et al. (2009) together with the data from Pearson & Mueller (1996). For gauche-C2H5OH, the data were taken from Pearson et al. (2008) together with the data from Pearson et al. (1996). For CH3CH2CN, the data were compiled from Pearson et al. (1994); Brauer et al. (2009). For SO2, the data were taken from Müller & Brünken (2005) with additional data from Lovas (1985); Helminger & De Lucia (1985); Belov et al. (1998).

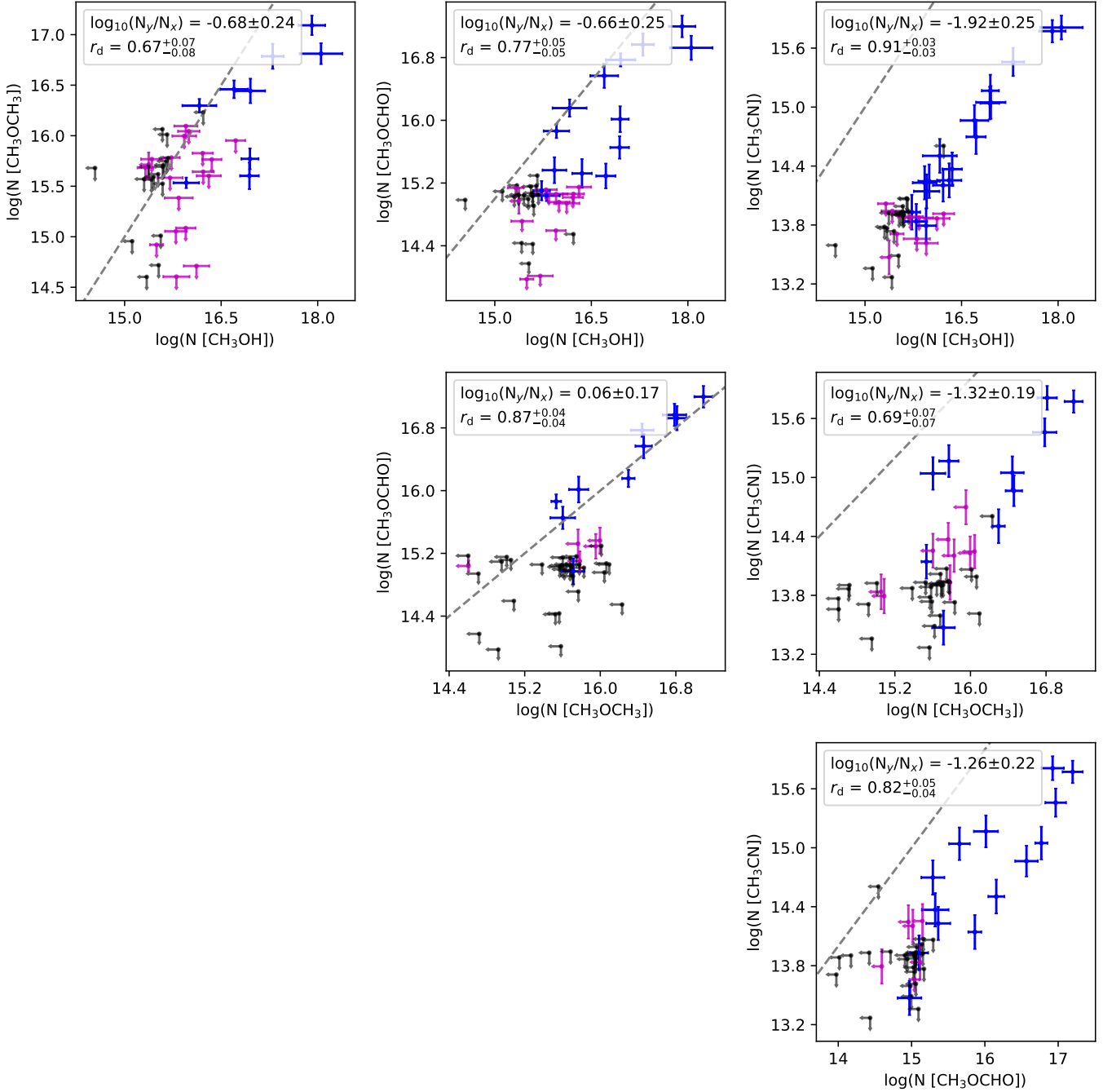


Figure 9. Corner plot of the correlations of the column densities between CH₃OH, CH₃CN, HCOOCH₃, and CH₃OCH₃. The color code follows that in Figure 7. The dashed line indicates equality. The legends indicate the Pearson's r for the detection-only sample (r_d) and the logarithmic ratio of the two molecules (N_y/N_x). The four most detected COMs are shown in this figure, while other COMs are shown in Figure 11.

B. IDENTIFIED SPECIES AND TRANSITIONS

Table ?? lists the species and their transitions identified from the PEACHES spectra.

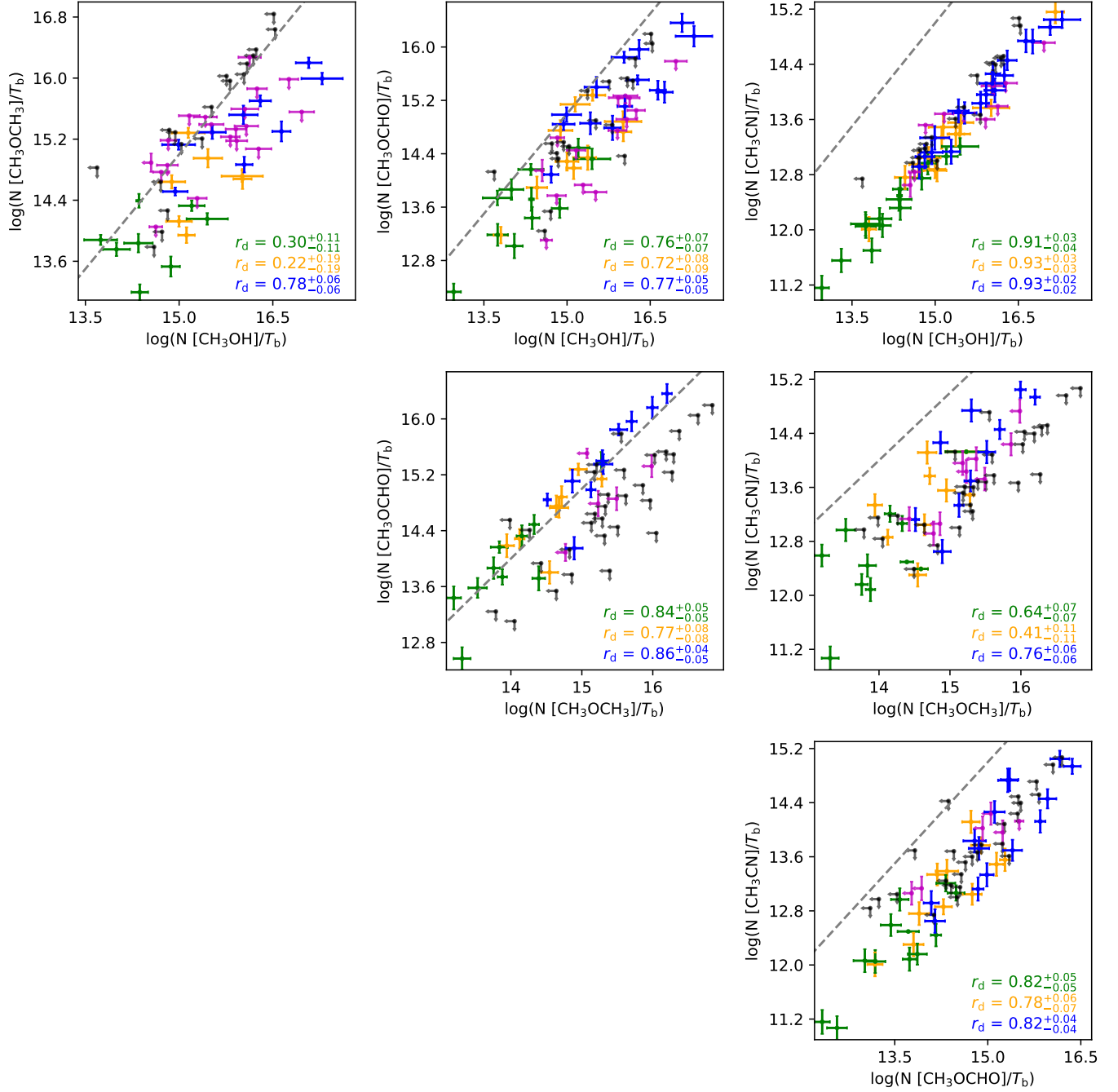


Figure 10. Corner plot of the correlations of the normalized column densities. The blue, magenta, and black symbols indicate the column densities normalized by the continuum brightness temperature ($T_{b,\text{cont}}$), while the color scheme follows that in Figure 7. The orange symbols show the column densities normalized by $T_{b,\text{cont}}$ and the bolometric luminosity (L_{bol}), while the green symbols show that normalized by $T_{b,\text{cont}}$ and the bolometric temperature (T_{bol}). We only show the column densities if both molecules are detected for the ones normalized by $T_{b,\text{cont}} T_{\text{bol}}$ and $T_{b,\text{cont}} L_{\text{bol}}$. The Pearson's r correlation coefficient for the detections with each normalization is shown in the legend with corresponding color. A few close multiple sources, including Per-emb 12 A & B, Per-emb 35 A & B, and Per-emb 11 A & C, are excluded for the normalization of T_{bol} and L_{bol} due to their poorly determined SEDs.

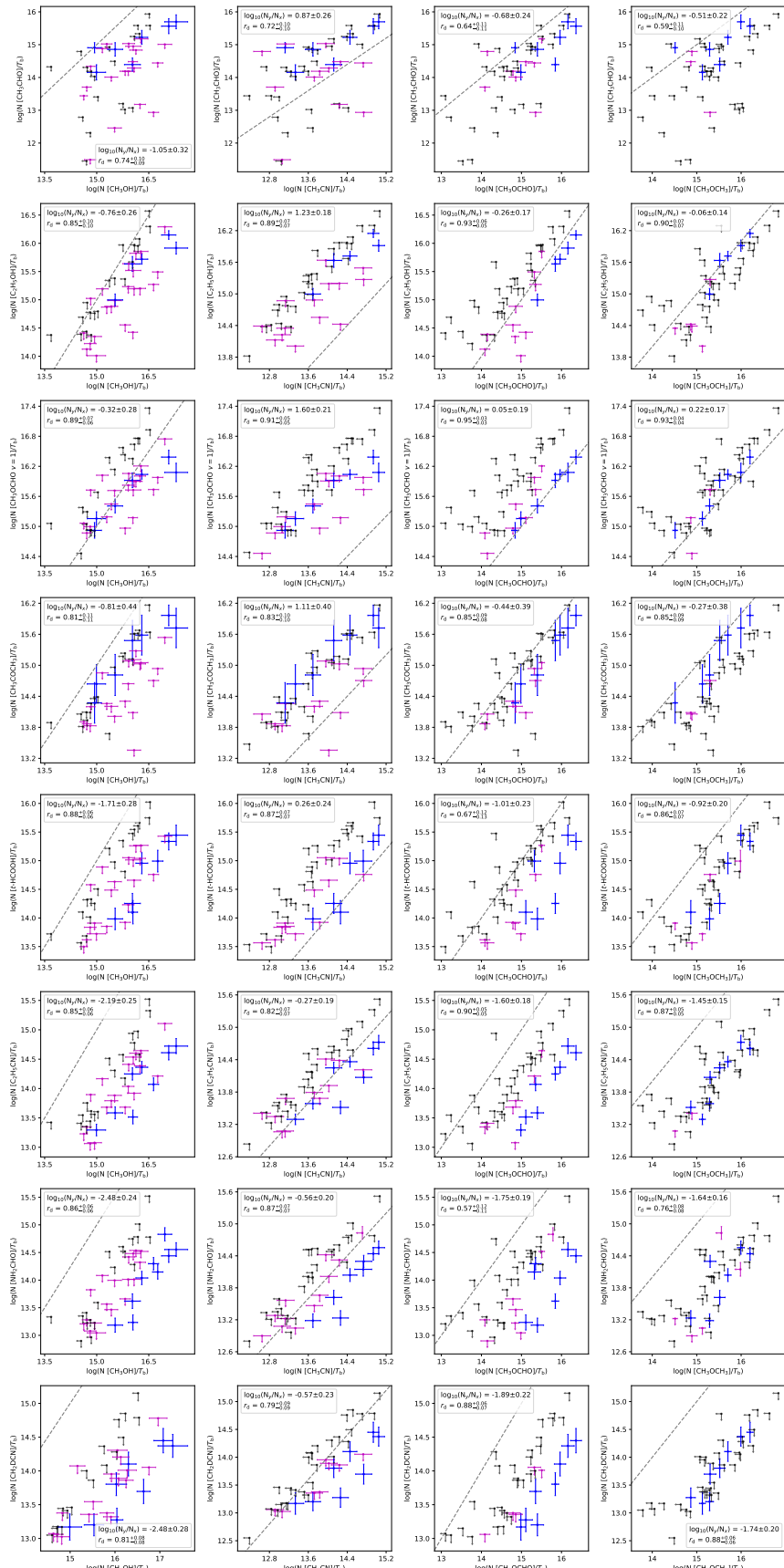


Figure 11. Corner plot of the correlations of the column densities normalized by the continuum brightness temperature between the more abundance COMs, CH_3OH , CH_3CN , HCOOCH_3 , and CH_3OCH_3 , and the less abundance COMs CH_3CHO , $\text{C}_2\text{H}_5\text{OH}$, $\text{HCOOCH}_3 v = 1$, CH_3COCH_3 , $\text{CH}_3\text{CH}_2\text{CN}$, $t\text{-HCOOH}$, and NH_2CHO . The legends are similar to Figure 7.

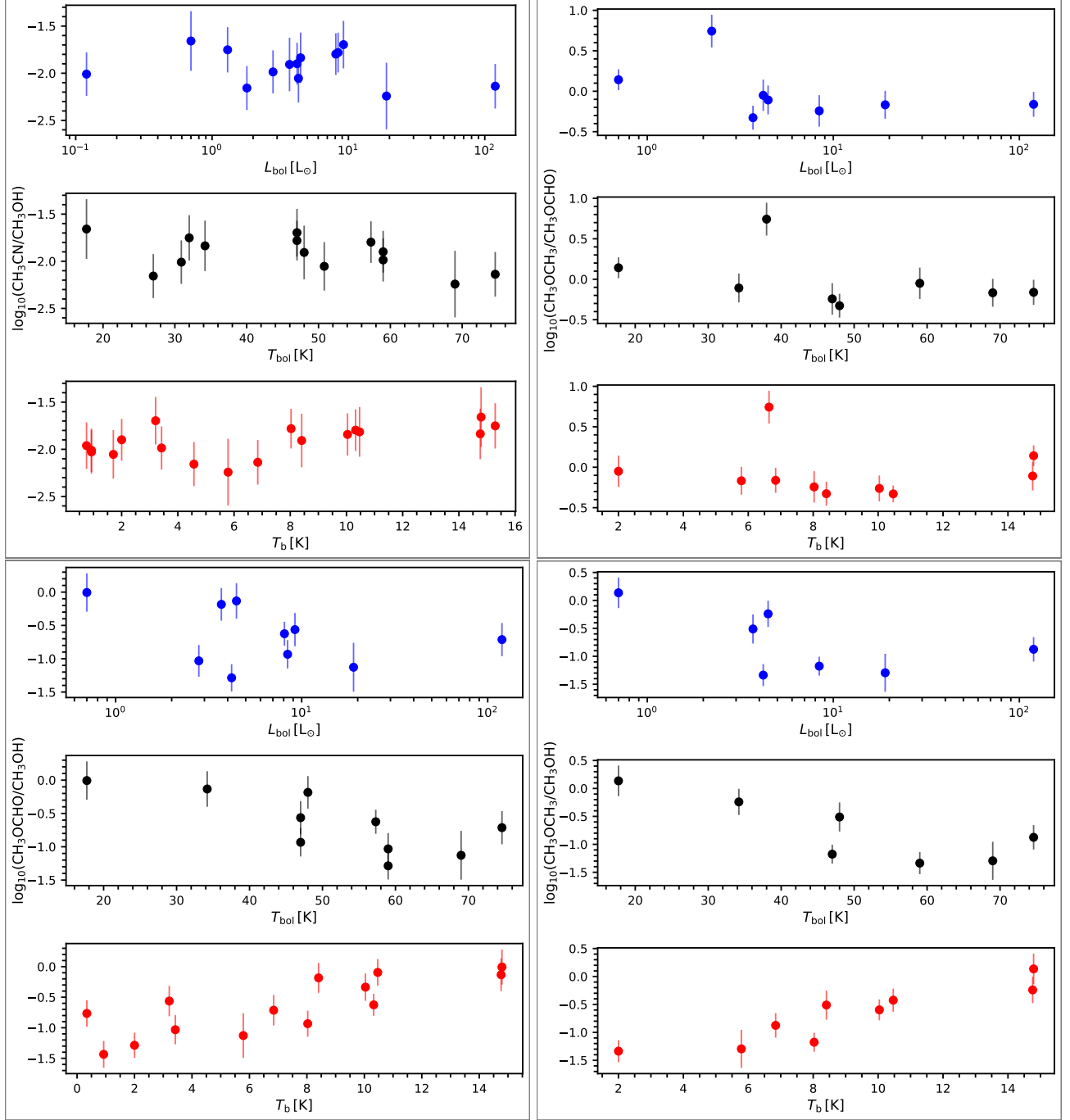


Figure 12. Ratios of well-detected molecules, CH_3OH , CH_3CN , HCOOCH_3 , and CH_3OCH_3 , as functions of L_{bol} (blue), T_{bol} (black), and T_b (red).

C. INTENSITY MAPS OF CH_3OH , CH_3CN , HCOOCH_3 , AND CH_3OCH_3

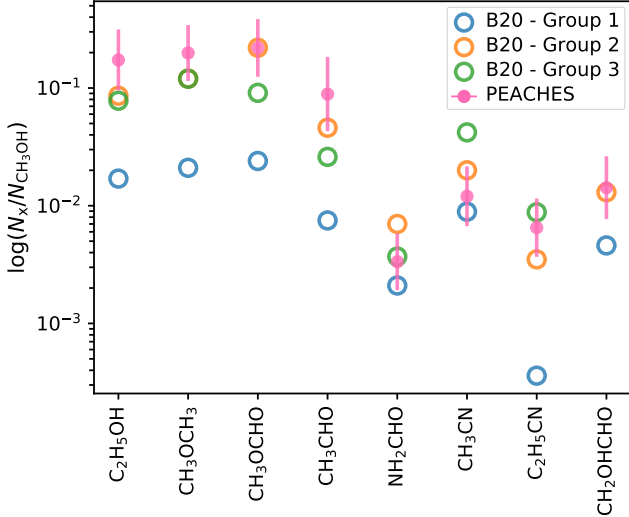


Figure 13. The ratios of the COMs commonly found in the PEACHES survey and the CALYPSO survey (Belloche et al. 2020), which categorize their sample into three groups according to their COMs abundance to CH_3OH . Group 3 has no detection of CH_2OHCHO .

D. THE SPECTRA OF C_2H

The C_2H spectra toward the continuum emission have irregular line profiles. Some spectra have strong self-absorption, while some spectra only show the blue-shifted emission. Due to the absorption and irregular line profile, the xCLASS fitting routine often fails to faithfully reproduce the observed C_2H spectra. C_2H can easily form in the outflow cavity wall due to the abundant CH_4 sublimated from dust grains as well as C^+ ionized by the UV radiation. Thus, the C_2H spectra can have broad line width and multiple components. Furthermore, the morphology of the C_2H emission traces the outflows, making our extraction from the continuum emission non-ideal for representing the nature of the C_2H emission. [Figure 16 and Y show the spectra and the moment 0 map of \$\text{C}_2\text{H}\$, respectively.](#)

REFERENCES

- Aikawa, Y. 2013, Chemical Reviews, 113, 8961
 Astropy Collaboration, Price-Whelan, A. M., Sipőcz, B. M., et al. 2018, AJ, 156, 123
 Belloche, A., Maury, A. J., Maret, S., et al. 2020, A&A, 635, A198
 Belov, S. P., Tretyakov, M. Y., Kozin, I. N., et al. 1998, Journal of Molecular Spectroscopy, 191, 17
 Bergner, J. B., Öberg, K. I., Garrod, R. T., & Graninger, D. M. 2017, ApJ, 841, 120
 Bottinelli, S., Ceccarelli, C., Williams, J. P., & Lefloch, B. 2007, A&A, 463, 601
 Bottinelli, S., Ceccarelli, C., Lefloch, B., et al. 2004, ApJ, 615, 354
 Brauer, C. S., Pearson, J. C., Drouin, B. J., & Yu, S. 2009, ApJS, 184, 133
 Carney, M. T., Yıldız, U. A., Mottram, J. C., et al. 2016, A&A, 586, A44
 Carvajal, M., Willaert, F., Demaison, J., & Kleiner, I. 2007, Journal of Molecular Spectroscopy, 246, 158
 Cazaux, S., Tielens, A. G. G. M., Ceccarelli, C., et al. 2003, ApJL, 593, L51
 Ceccarelli, C. 2004, in Astronomical Society of the Pacific Conference Series, Vol. 323, Star Formation in the Interstellar Medium: In Honor of David Hollenbach, ed. D. Johnstone, F. C. Adams, D. N. C. Lin, D. A. Neufeld, & E. C. Ostriker, 195
 Curtis, E. I., Richer, J. S., Swift, J. J., & Williams, J. P. 2010, MNRAS, 408, 1516
 De Simone, M., Ceccarelli, C., Codella, C., et al. 2020, ApJL, 896, L3
 Dunham, M. M., Arce, H. G., Allen, L. E., et al. 2013, AJ, 145, 94
 Endres, C. P., Drouin, B. J., Pearson, J. C., et al. 2009, A&A, 504, 635

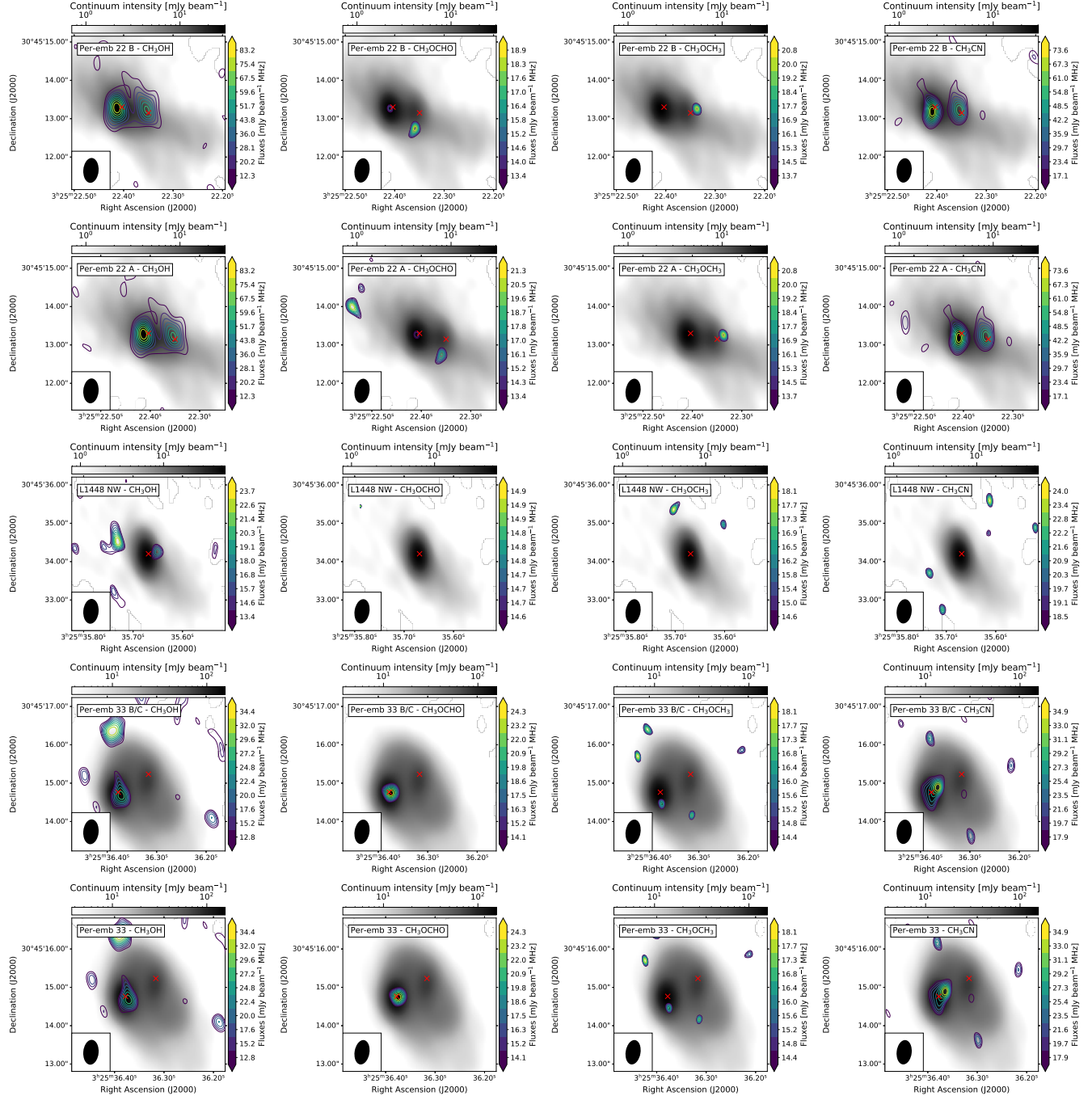


Figure 14. The intensity maps of most detected COMs, CH_3OH , CH_3CN , HCOOCH_3 , and CH_3OCH_3 (from left to right). Each row shows the emission of a PEACHES protostar with increasing R.A. The intensity is calculated by integrating over 3 km s^{-1} around the line centroid, while the lowest contour shows the 3σ value. The grayscale images illustrate the continuum emission.

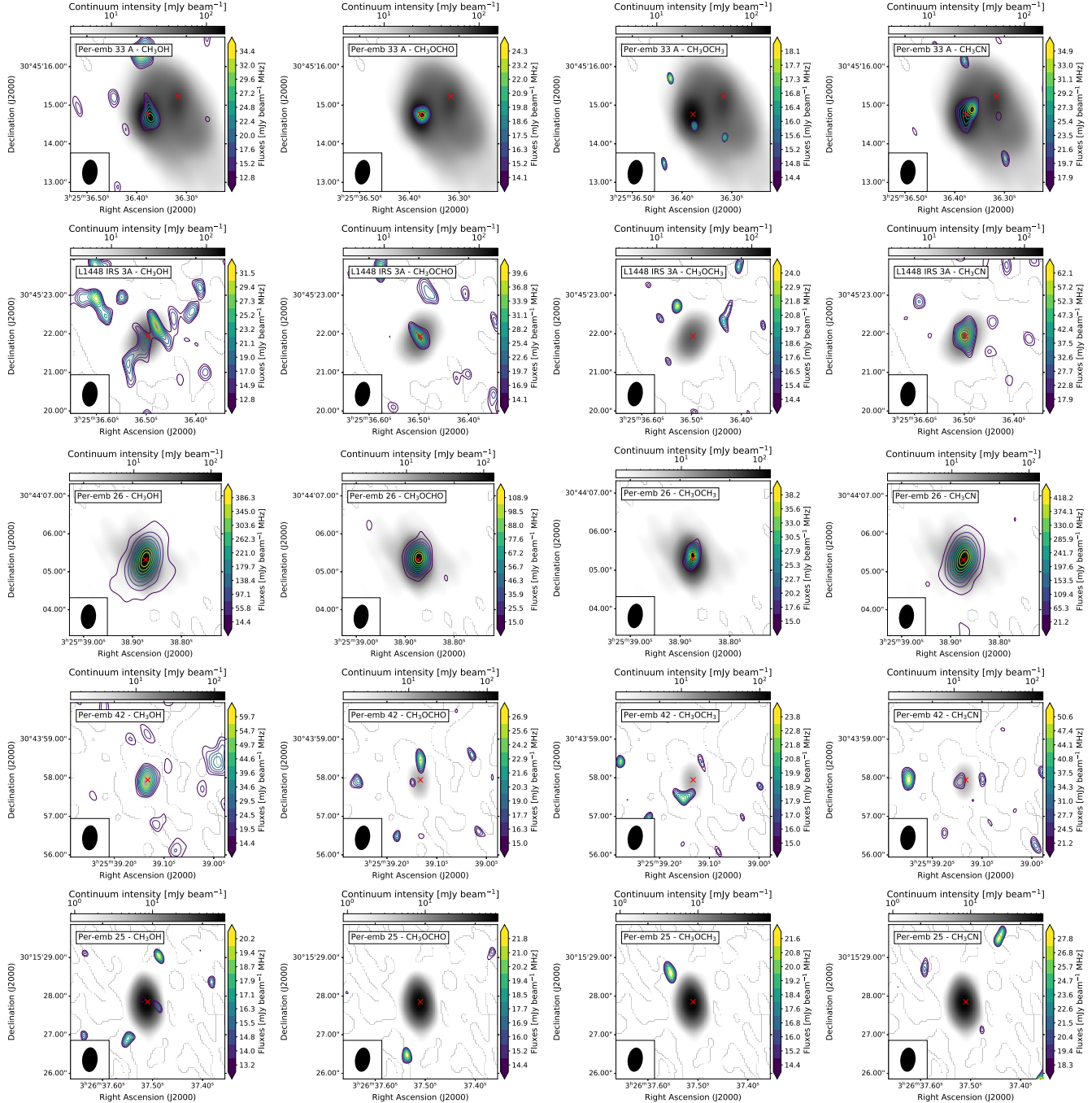


Figure 14 (Cont.).

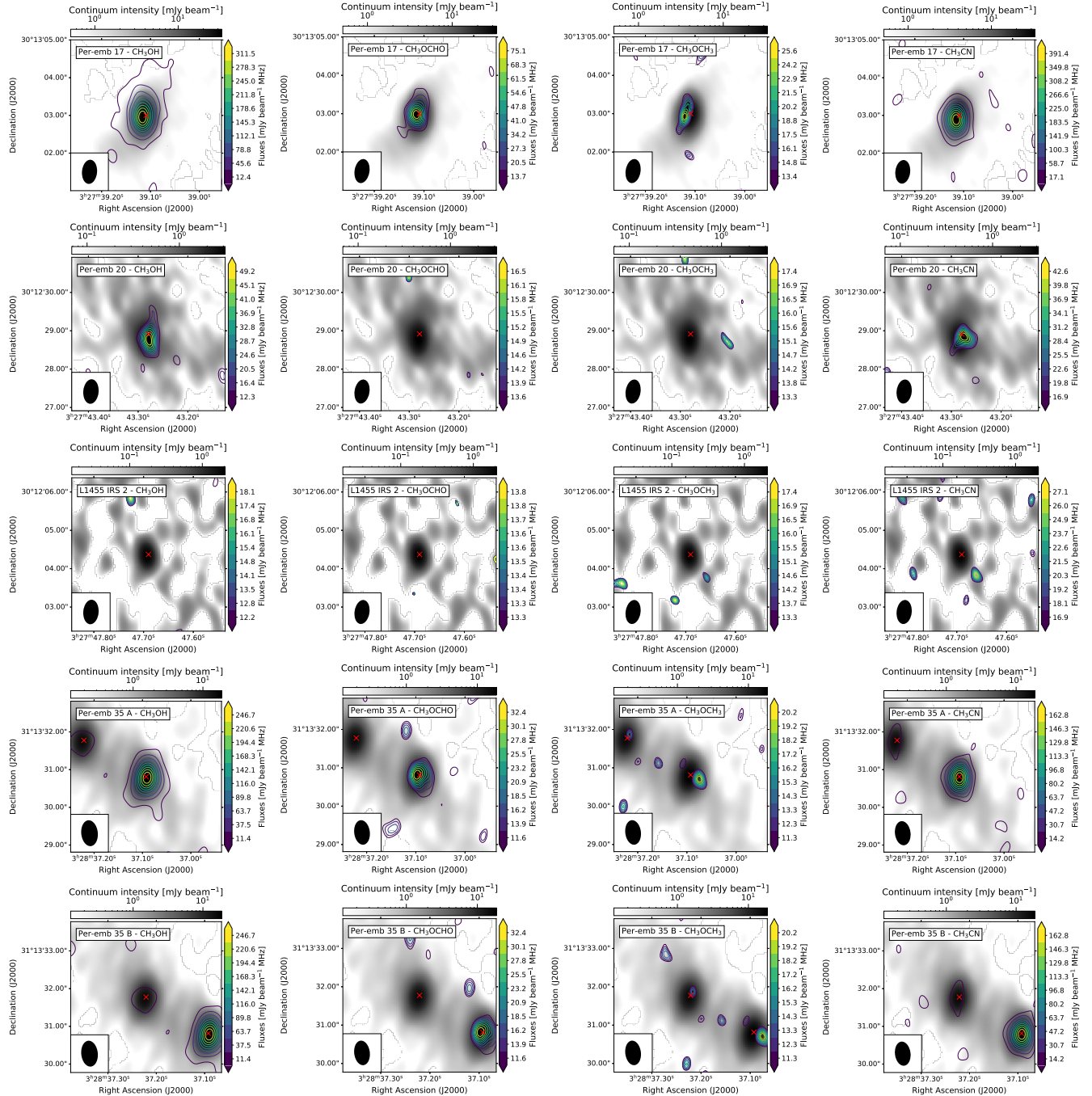


Figure 14 (Cont.).

- Endres, C. P., Schlemmer, S., Schilke, P., Stutzki, J., & Müller, H. S. P. 2016, Journal of Molecular Spectroscopy, 327, 95
- Garrod, R. T., Widicus Weaver, S. L., & Herbst, E. 2008, ApJ, 682, 283
- Gerin, M., Pety, J., Commerçon, B., et al. 2017, A&A, 606, A35
- Graninger, D. M., Wilkins, O. H., & Öberg, K. I. 2016, ApJ, 833, 125

- Gratier, P., Majumdar, L., Ohishi, M., et al. 2016, ApJS, 225, 25
- Groner, P., Albert, S., Herbst, E., et al. 2002, ApJS, 142, 145
- Hatchell, J., Fuller, G. A., Richer, J. S., Harries, T. J., & Ladd, E. F. 2007, A&A, 468, 1009
- Hatchell, J., Richer, J. S., Fuller, G. A., et al. 2005, A&A, 440, 151

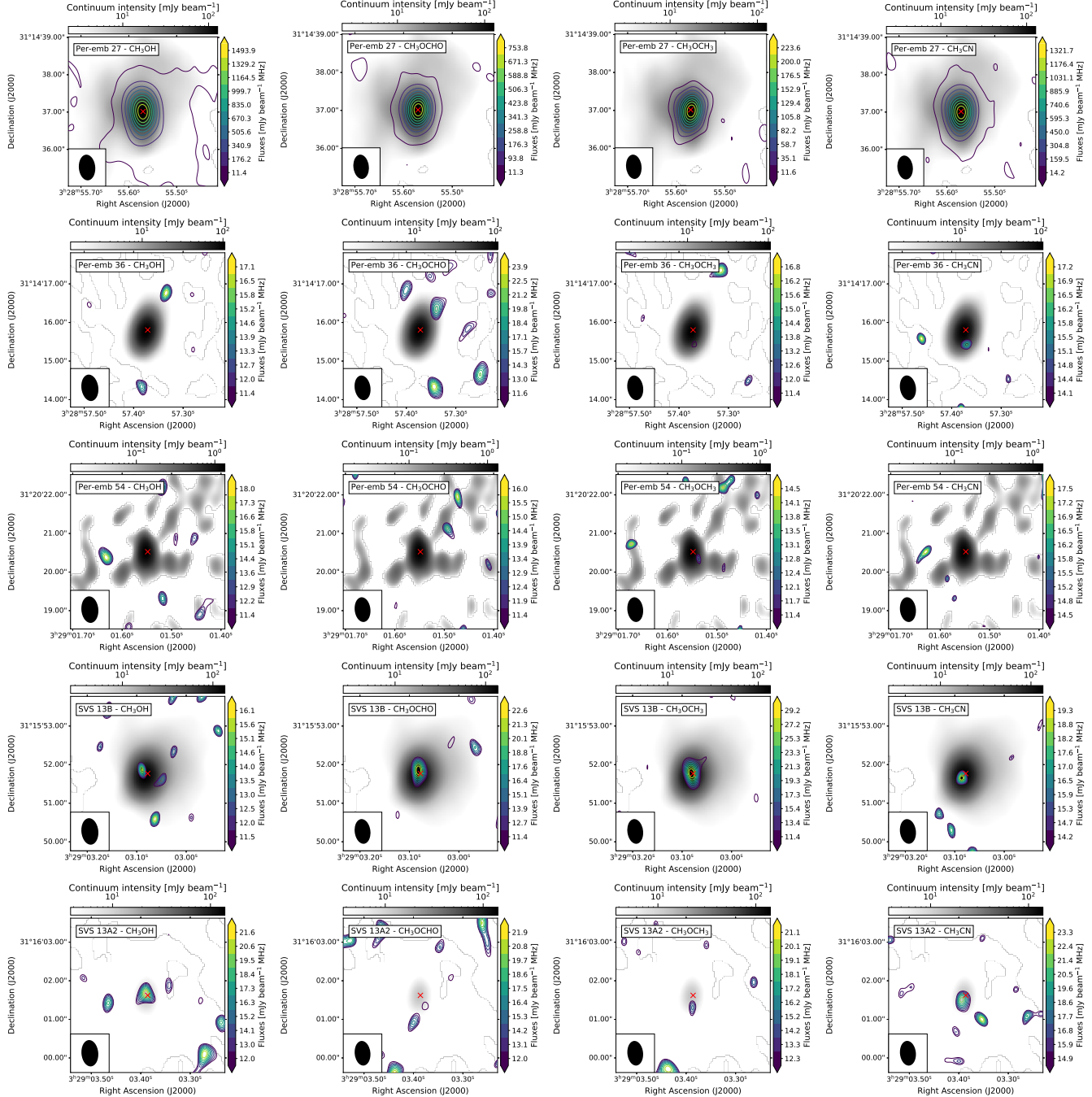


Figure 14 (Cont.).

- Helmlinger, P. A., & De Lucia, F. C. 1985, Journal of Molecular Spectroscopy, 111, 66
- Higuchi, A. E., Sakai, N., Watanabe, Y., et al. 2018, ApJS, 236, 52
- Hirota, T., Bushimata, T., Choi, Y. K., et al. 2008, PASJ, 60, 37
- Ilyushin, V., Kryvda, A., & Alekseev, E. 2009, Journal of Molecular Spectroscopy, 255, 32
- Imai, M., Oya, Y., Sakai, N., et al. 2019, ApJL, 873, L21

- Imai, M., Sakai, N., Oya, Y., et al. 2016, ApJL, 830, L37
- Jørgensen, J. K., Belloche, A., & Garrod, R. T. 2020, arXiv e-prints, arXiv:2006.07071
- Jørgensen, J. K., Johnstone, D., Kirk, H., et al. 2008, ApJ, 683, 822
- Jørgensen, J. K., van der Wiel, M. H. D., Coutens, A., et al. 2016, A&A, 595, A117
- Kleiner, I., Lovas, F. J., & Godefroid, M. 1996, Journal of Physical and Chemical Reference Data, 25, 1113

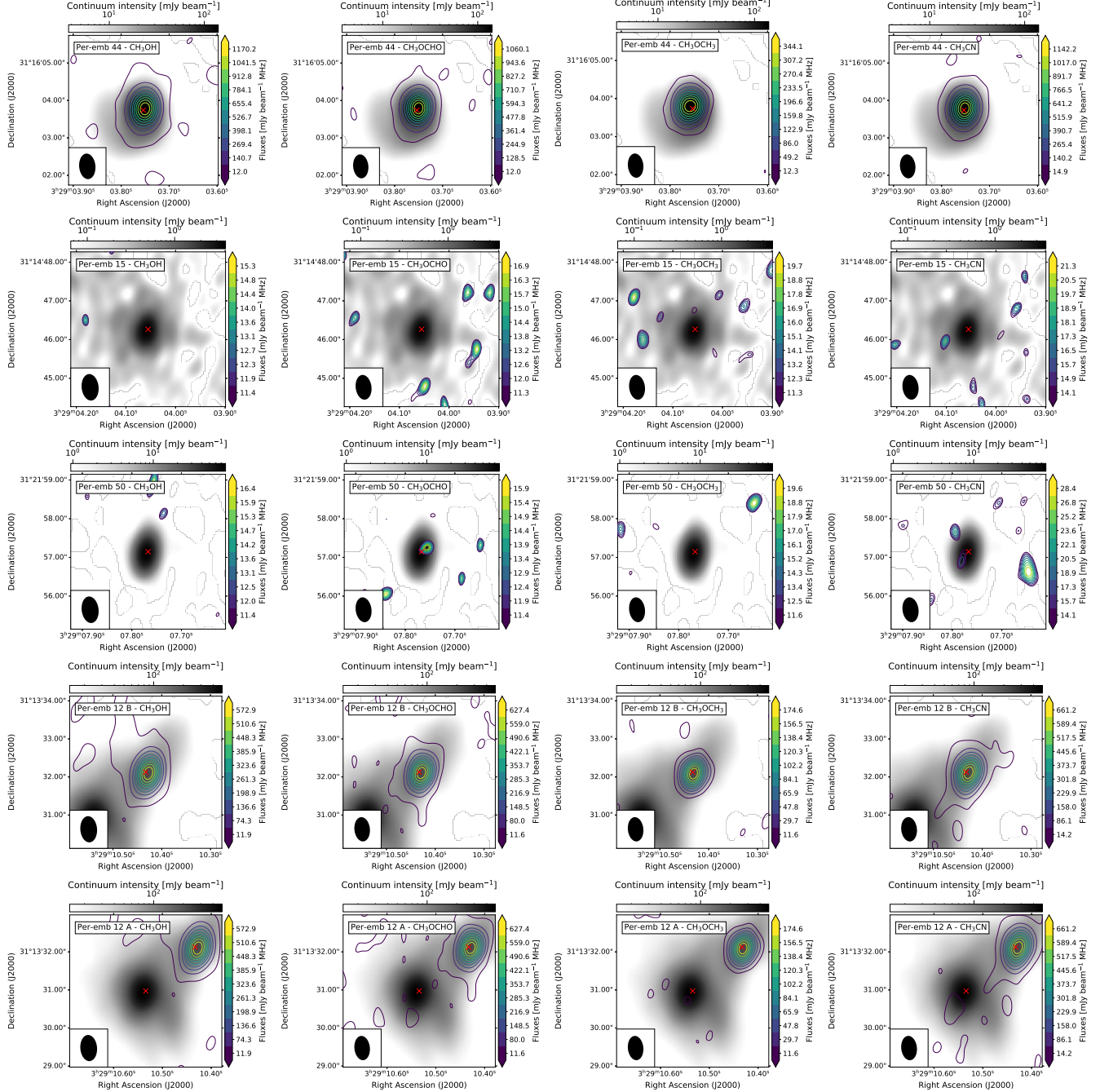


Figure 14 (Cont.).

- Ko, C.-L., Liu, H. B., Lai, S.-P., et al. 2020, ApJ, 889, 172
 Law, C. J., Öberg, K. I., Bergner, J. B., & Graninger, D. 2018, ApJ, 863, 88
 Lee, C.-F., Li, Z.-Y., Ho, P. T. P., et al. 2017, ApJ, 843, 27
 Lovas, F. J. 1985, Journal of Physical and Chemical Reference Data, 14, 395
 Maeda, A., De Lucia, F. C., & Herbst, E. 2008, Journal of Molecular Spectroscopy, 251, 293

- Marcelino, N., Gerin, M., Cernicharo, J., et al. 2018, A&A, 620, A80
 McGuire, B. A. 2018, ApJS, 239, 17
 McMullin, J. P., Waters, B., Schiebel, D., Young, W., & Golap, K. 2007, in Astronomical Society of the Pacific Conference Series, Vol. 376, Astronomical Data Analysis Software and Systems XVI, ed. R. A. Shaw, F. Hill, & D. J. Bell, 127
 Möller, T., Endres, C., & Schilke, P. 2017, A&A, 598, A7

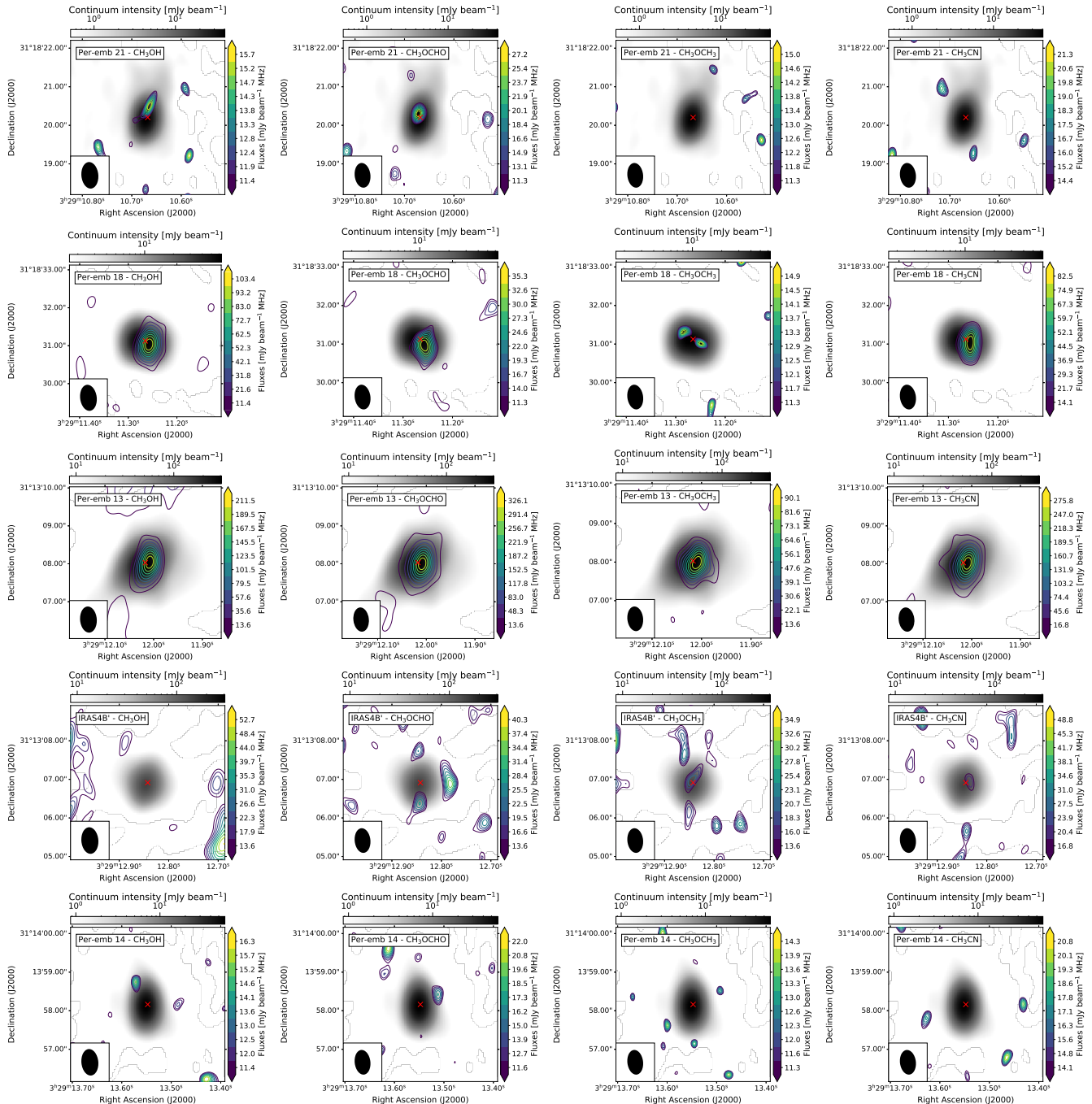


Figure 14 (Cont.).

Müller, H. S. P., & Brünken, S. 2005, Journal of Molecular Spectroscopy, 232, 213

Müller, H. S. P., Drouin, B. J., & Pearson, J. C. 2009, A&A, 506, 1487

Müller, H. S. P., Schlöder, F., Stutzki, J., & Winnewisser, G. 2005, Journal of Molecular Structure, 742, 215

Müller, H. S. P., Thorwirth, S., Roth, D. A., & Winnewisser, G. 2001, A&A, 370, L49

Murillo, N. M., van Dishoeck, E. F., Tobin, J. J., & Fedele, D. 2016, A&A, 592, A56

Nagy, Z., Spezzano, S., Caselli, P., et al. 2019, A&A, 630, A136

Oesterling, L. C., Albert, S., De Lucia, F. C., Sastry, K. V. L. N., & Herbst, E. 1999, ApJ, 521, 255

Ortiz-León, G. N., Loinard, L., Dzib, S. A., et al. 2018, ApJ, 865, 73

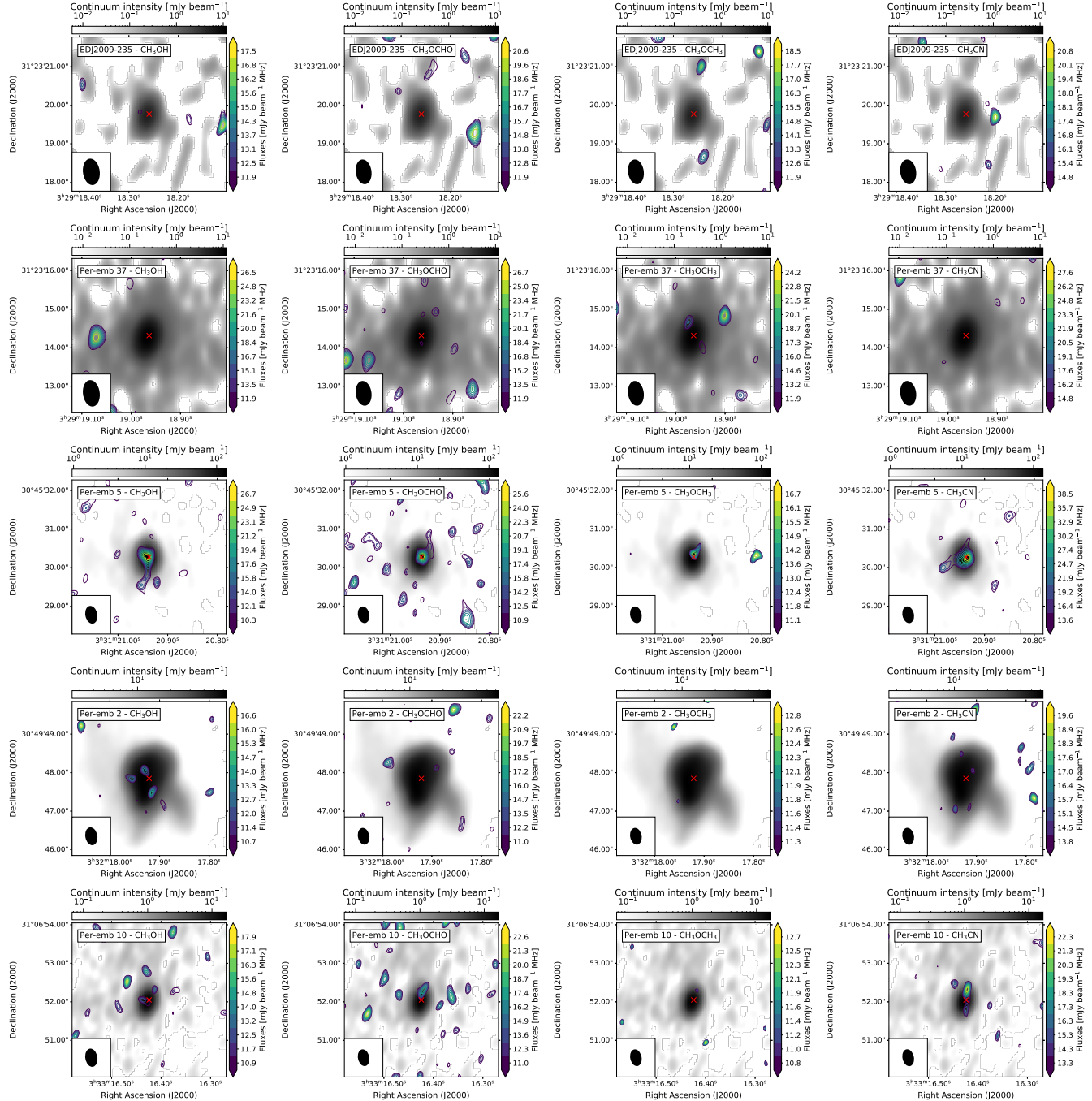


Figure 14 (Cont.).

- Oya, Y., Sakai, N., López-Sepulcre, A., et al. 2016, ApJ, 824, 88
 Oya, Y., Sakai, N., Watanabe, Y., et al. 2017, ApJ, 837, 174
 Pearson, J. C., Brauer, C. S., & Drouin, B. J. 2008, Journal of Molecular Spectroscopy, 251, 394
 Pearson, J. C., & Mueller, H. S. P. 1996, ApJ, 471, 1067
 Pearson, J. C., Sastry, K. V. L. N., Herbst, E., & De Lucia, F. C. 1994, ApJS, 93, 589
 —. 1996, Journal of Molecular Spectroscopy, 175, 246

- Pearson, J. C., Yu, S., & Drouin, B. J. 2012, Journal of Molecular Spectroscopy, 280, 119
 Pickett, H. M., Poynter, R. L., Cohen, E. A., et al. 1998, JQSRT, 60, 883
 Plummer, G. M., Herbst, E., De Lucia, F., & Blake, G. A. 1984, ApJS, 55, 633
 Rabli, D., & Flower, D. R. 2010, MNRAS, 406, 95

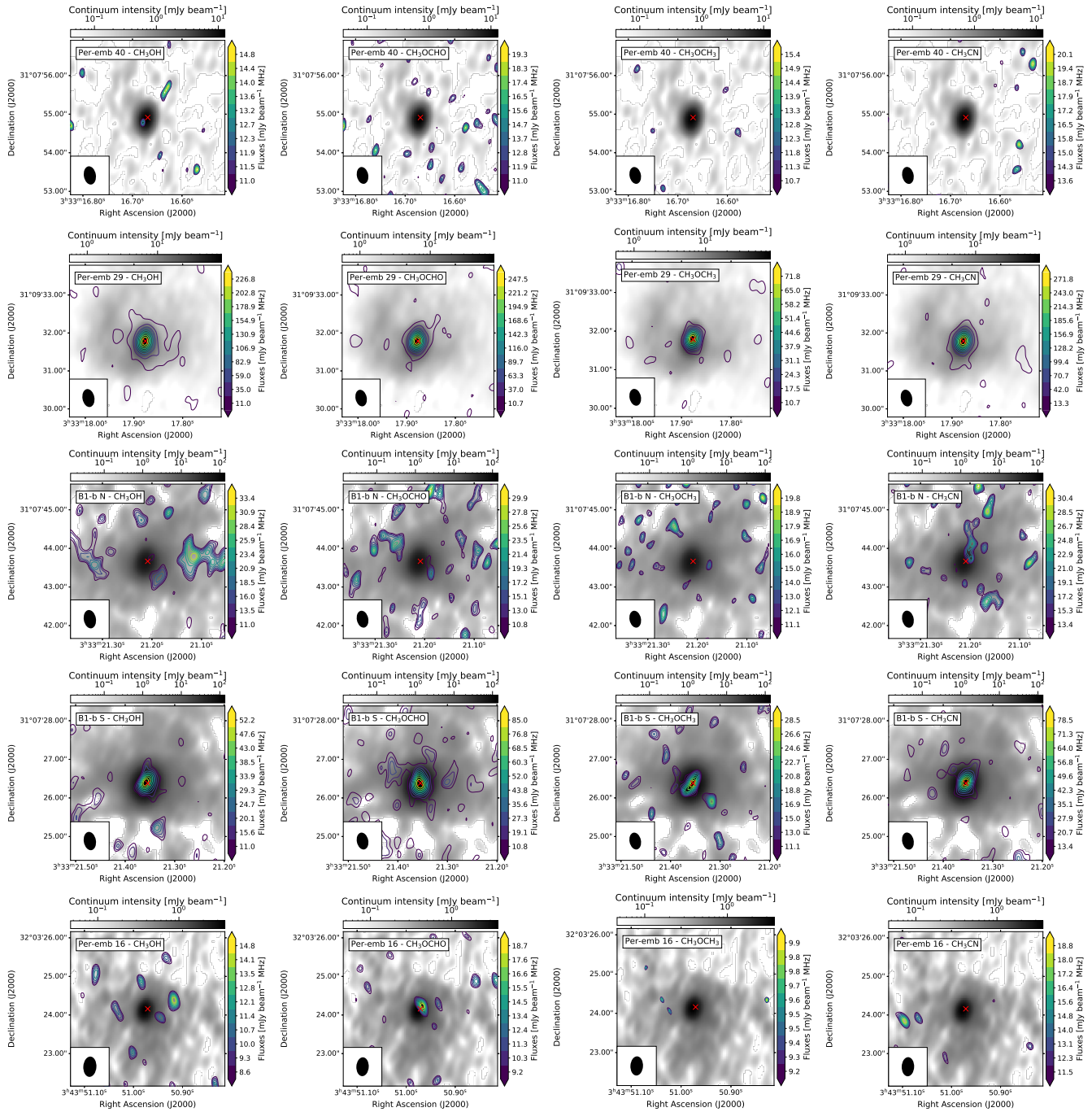


Figure 14 (Cont.).

- Robitaille, T., Ginsburg, A., Beaumont, C., Leroy, A., & Rosolowsky, E. 2016, spectral-cube: Read and analyze astrophysical spectral data cubes, , ascl:1609.017
- Sahu, D., Liu, S.-Y., Su, Y.-N., et al. 2019, ApJ, 872, 196
- Sakai, N., Sakai, T., Hirota, T., Burton, M., & Yamamoto, S. 2009, ApJ, 697, 769
- Sakai, N., Sakai, T., Hirota, T., & Yamamoto, S. 2010, ApJ, 722, 1633

- Sakai, N., & Yamamoto, S. 2013, Chemical Reviews, 113, 8981
- Sakai, N., Sakai, T., Hirota, T., et al. 2014, Nature, 507, 78
- Sakai, N., Oya, Y., López-Sepulcre, A., et al. 2016, ApJL, 820, L34
- Schöier, F. L., van der Tak, F. F. S., van Dishoeck, E. F., & Black, J. H. 2005, A&A, 432, 369
- Stephens, I. W., Dunham, M. M., Myers, P. C., et al. 2018, ApJS, 237, 22

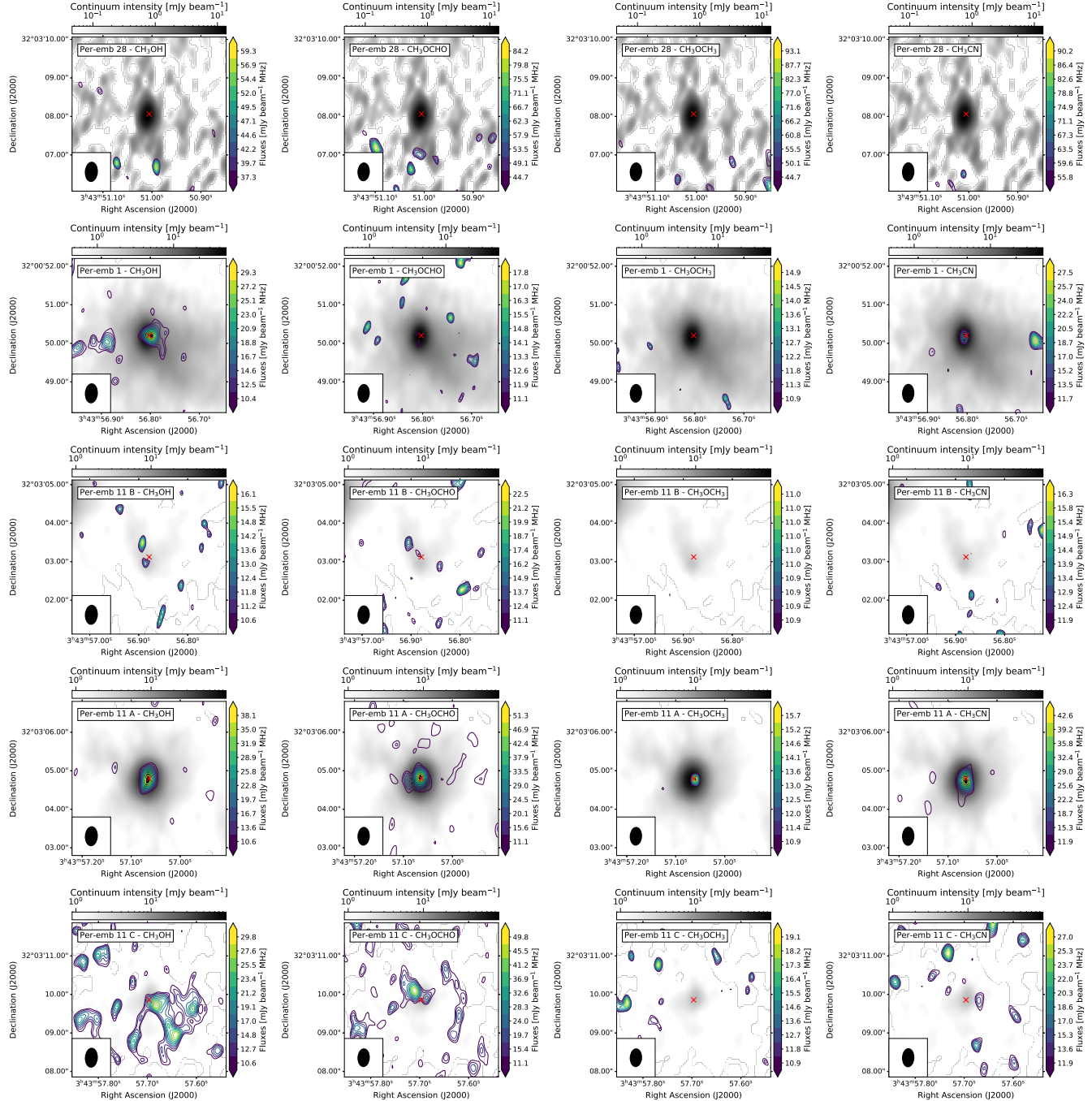


Figure 14 (Cont.).

- Stephens, I. W., Bourke, T. L., Dunham, M. M., et al. 2019, ApJS, 245, 21
- Tobin, J. J., Looney, L. W., Li, Z.-Y., et al. 2016, ApJ, 818, 73
- Tychoniec, L., Tobin, J. J., Karska, A., et al. 2018, ApJS, 238, 19
- Tychoniec, L., Manara, C. F., Rosotti, G. P., et al. 2020, arXiv e-prints, arXiv:2006.02812

- Xu, L.-H., & Lovas, F. J. 1997, Journal of Physical and Chemical Reference Data, 26, 17
- Xu, L.-H., Fisher, J., Lees, R. M., et al. 2008, Journal of Molecular Spectroscopy, 251, 305
- Yang, Y.-L., Evans, Neal J., I., Green, J. D., Dunham, M. M., & Jørgensen, J. K. 2017, ApJ, 835, 259
- Yang, Y.-L., Evans, Neal J., I., Smith, A., et al. 2020, ApJ, 891, 61

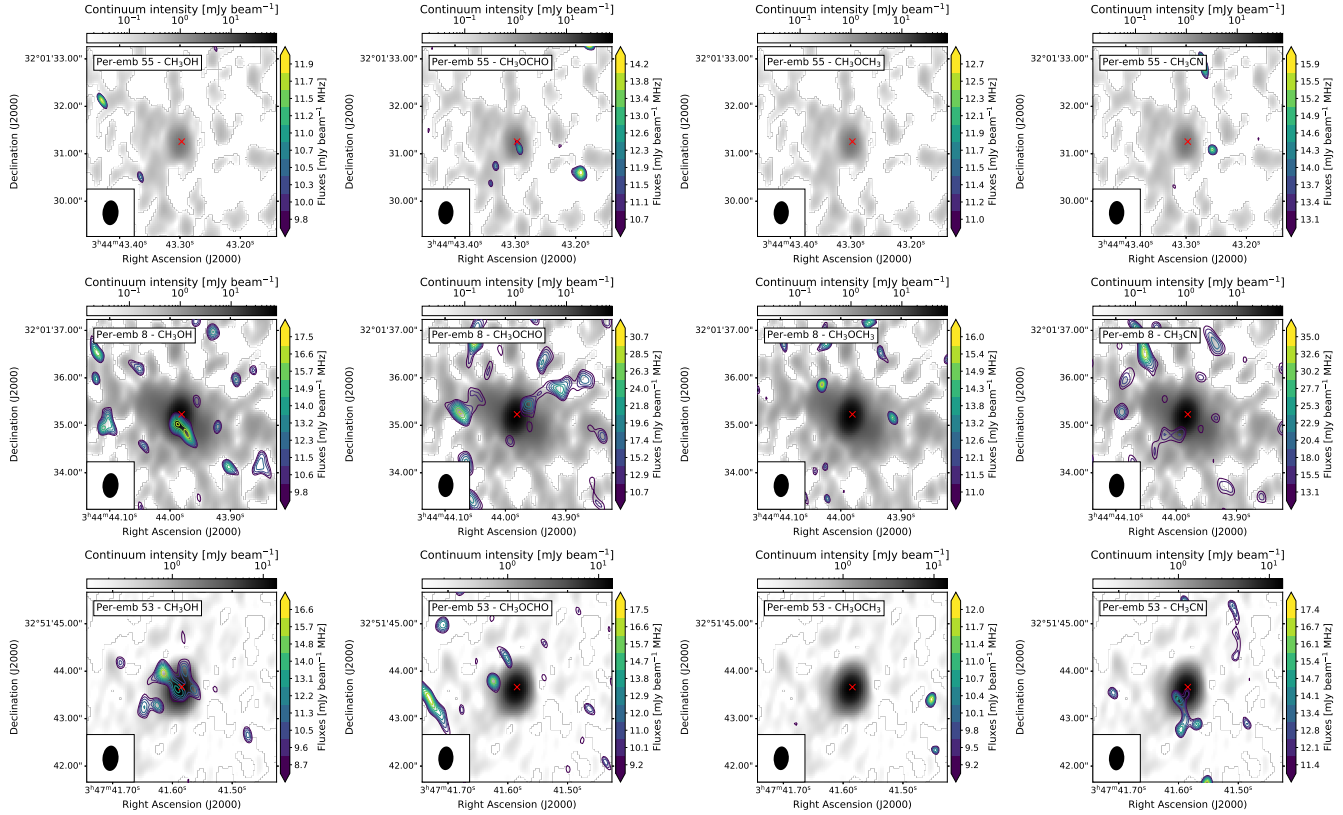


Figure 14 (Cont.).

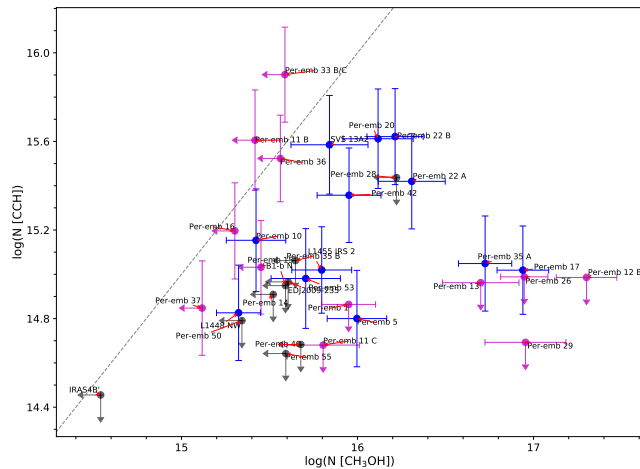


Figure 15. Correlation of the column densities of C₂H and CH₃OH fitted from the PEACHES protostars. The sources where both molecules are detected are shown in black; the sources where only one molecule is detected are shown in magenta; finally, the sources where both molecules are not detected are shown in black for the corresponding upper limits.

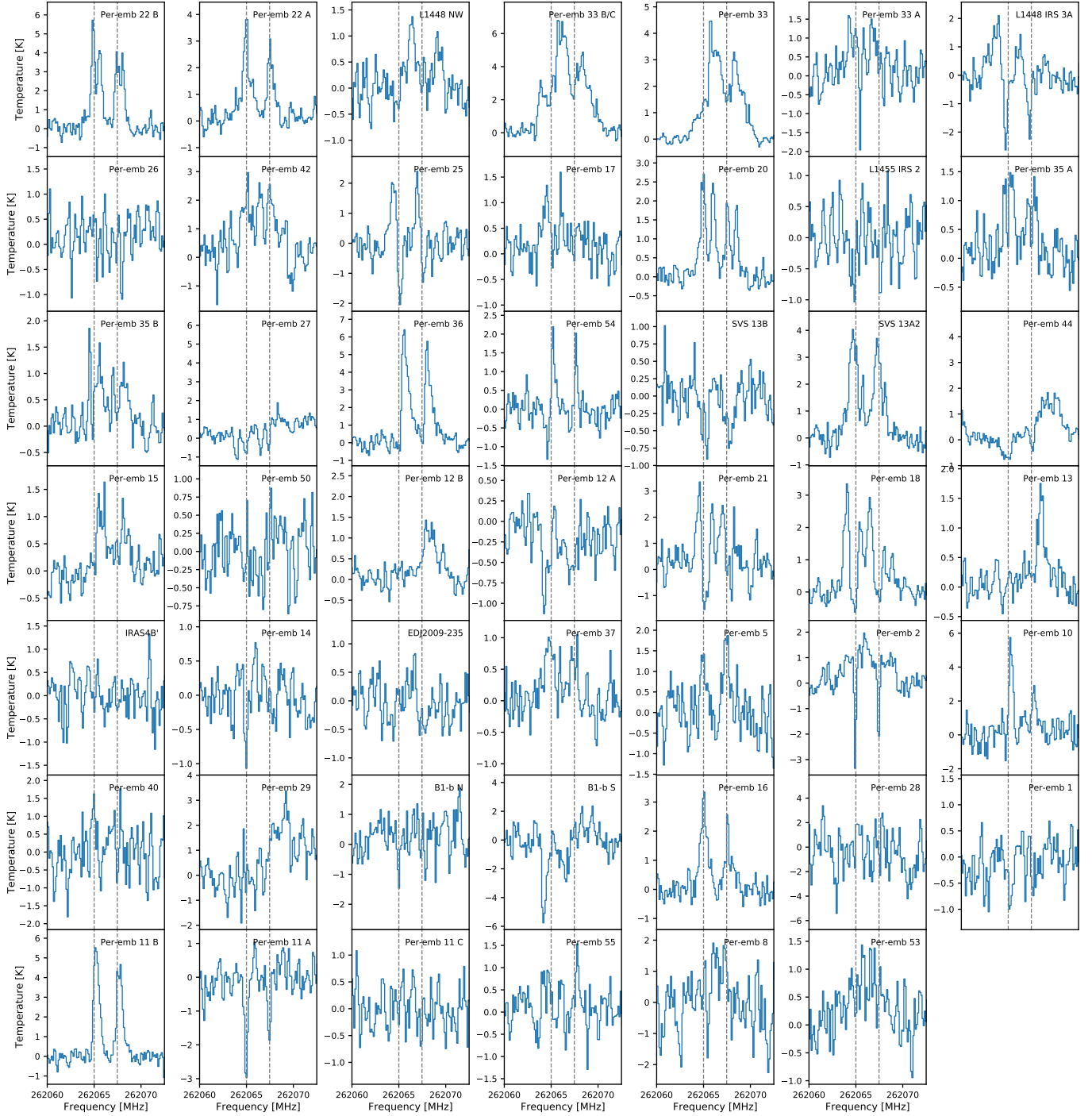


Figure 16. The C₂H spectra of all PEACHES sources extracted from the continuum emission.

- Zhang, Y., Higuchi, A. E., Sakai, N., et al. 2018, ApJ, 864,
76
- Zucker, C., Speagle, J. S., Schlafly, E. F., et al. 2020, A&A,
633, A51